NUCL SCI TECH (2020) 31:102
https://doi.org/10.1007/s41365-020-00805-7

Methodology development and application of X-ray imaging beamline at SSRF

Hong-Lan Xie[1,2] · Biao Deng[1,2] · Guo-Hao Du[1,2] · Ya-Nan Fu[1,2] · Han Guo[1,2] · Yan-Ling Xue[1,2] · Guan-Yun Peng[1,2] · Fen Tao[1,2] · Ling Zhang[1,2] · Ti-Qiao Xiao[1,2]

Received: 12 June 2020 / Revised: 2 August 2020 / Accepted: 6 August 2020 / Published online: 11 October 2020

Abstract This paper introduces some latest developments regarding the X-ray imaging methodology and applications of the X-ray imaging and biomedical application beamline (BL13W1) at Shanghai Synchrotron Radiation Facility in the past 5 years. The photon energy range of the beamline is 8–72.5 keV. Several sets of X-ray imaging detectors with different pixel sizes (0.19–24 μm) are used to realize X-ray microcomputed tomography (X-ray micro-CT) and X-ray in-line phase-contrast imaging. To satisfy the requirements of user experiments, new X-ray imaging methods and image processing techniques are developed. In vivo dynamic micro-CT experiments with living insects are performed in 0.5 s (sampling rate of 2 Hz, 2 tomograms/s) with a monochromatic beam from a wiggler source and in 40 ms (sampling rate of 25 Hz, 25 tomograms/s) with a white beam from a bending magnet source. A new X-ray imaging method known as move contrast X-ray imaging is proposed, with which blood flow and moving tissues in raw images can be distinguished according to their moving frequencies in the time domain. Furthermore, X-ray speckle-tracking imaging with twice exposures to eliminate the edge enhancement effect is developed. A high-precision quantification method is realized to measure complex three-dimensional blood vessels obtained via X-ray micro-CT. X-ray imaging methods such as three-dimensional X-ray diffraction microscopy, small-angle X-ray scattering CT, and X-ray fluorescence CT are developed, in which the X-ray micro-CT imaging method is combined with other contrast mechanisms such as diffraction, scattering, and fluorescence contrasts respectively. Moreover, an X-ray nano-CT experiment is performed with a 100 nm spatial resolution. Typical user experimental results from the fields of material science, biomedicine, paleontology, physics, chemistry, and environmental science obtained on the beamline are provided.

Keywords X-ray imaging · X-ray in-line phase-contrast imaging · X-ray micro-CT · Dynamic micro-CT · X-ray speckle-tracking imaging · 3DXRD · SAXS-CT · X-ray fluorescence CT · X-ray nano-CT · Move contrast X-ray imaging

1 Introduction

The X-ray imaging and biomedical applications beamline (BL13W1) at Shanghai Synchrotron Radiation Facility (SSRF) is mainly engaged in the developments and applications of X-ray in-line phase-contrast imaging, X-ray micro-computed tomography (X-ray micro-CT), and other new X-ray imaging methods. Since May 6, 2009, the BL13W1 beamline with 8–72.5 keV X-rays has been

This work was supported by the National Key Research and Development Program of China (Nos. 2017YFA0403801, 2016YFA0401302, 2017YFA0206004, 2018YFC1200204), and the National Major Scientific Instruments and Equipment Development Project of China (No. 11627901).

✉ Hong-Lan Xie
xiehonglan@sinap.ac.cn

✉ Ti-Qiao Xiao
tqxiao@sinap.ac.cn

[1] Shanghai Institute of Applied Physics, Chinese Academy of Sciences, Shanghai 201800, China

[2] Shanghai Synchrotron Radiation Facility (SSRF), Shanghai Advanced Research Institute, Chinese Academy of Sciences, Shanghai 201204, China

officially available to users. For X-ray micro-CT and X-ray in-line phase-contrast imaging, several sets of X-ray imaging detectors with different pixel sizes are provided (0.19–24 μm). A detailed introduction of the beamline including the developments of the X-ray imaging methodology and user research results since its opening is available in [1].

This paper introduces some latest developments on the X-ray imaging methodology and applications of the X-ray imaging and biomedical application beamline (BL13W1) at SSRF in the past 5 years. The photon energy range of the beamline is 8–72.5 keV. Several sets of X-ray imaging detectors with different pixel sizes (0.19–24 μm) are used to realize X-ray micro-computed tomography (X-ray micro-CT) and X-ray in-line phase-contrast imaging. To satisfy the new requirements of user experiments, new X-ray imaging methods and image processing techniques were developed. In vivo dynamic micro-CT experiments with living insects were realized in 0.5 s (sampling rate of 2 Hz, 2 tomograms/s) with a monochromatic beam from a wiggler source and in 40 ms (sampling rate of 25 Hz, 25 tomograms/s) with a white beam from a bending magnet source. A new X-ray imaging method known as move contrast X-ray imaging (MCXI) was proposed, with which the blood flow and moving tissues in raw images can be distinguished according to their moving frequencies in the time domain. Furthermore, X-ray speckle-tracking imaging with twice exposures to eliminate the edge enhancement effect was developed. A high-precision quantification method was realized to measure complex three-dimensional (3D) blood vessels obtained via X-ray micro-CT. X-ray imaging methods such as three-dimensional X-ray diffraction (3DXRD) microscopy, small-angle X-ray scattering CT (SAXS-CT), and X-ray fluorescence CT (XFCT) have been developed, in which the X-ray micro-CT imaging method was combined with other contrast mechanisms, such as diffraction, scattering, and fluorescence contrasts respectively. Moreover, an X-ray nano-CT experiment was performed with 100 nm spatial resolution. Typical user experimental results from the fields of material science, biomedicine, paleontology, physics, chemistry, and environmental science obtained on the beamline will be introduced herein.

2 Methodology developments

Some latest developments on the X-ray imaging methodology of BL13W1 will be introduced in this section.

2.1 Dynamic micro-CT

Dynamic X-ray micro-CT is an important tool for investigating the dynamic behaviors of materials because it can visualize the 3D microstructural evolution of materials in real time. A dynamic X-ray micro-CT system with a monochromatic X-ray beam from a wiggler source was set up. It comprised a Hamamatsu ORCA-Flash4.0 detector with a pixel size of 6.5 μm and an air bearing rotation stage with a maximum speed of 360°/s. An in vivo X-ray micro-CT experiment with a living bell cricket as the sample was performed on the system. The dynamic evolution of the 3D structure of the air sac of the insect was observed [2]. Each CT dataset of 136 projections was completed in 0.5 s, and 150 datasets were obtained. The maximum full frame rate of the detector was 100 frames/s (at 2048 × 2048 pixels). In this experiment, the region of interest was reduced to 2048 × 700 pixels (horizontal × vertical); therefore, the frame rate can be increased to 272 frames/s (136 projections in 0.5 s). Data were processed using the PITRE software package for phase-sensitive X-ray image processing and tomography reconstruction [3]. Using this reconstruction software, the CT reconstruction can yield good reconstructed images with a few projections (no less than 100 projections). The detector was equipped with a Camera Link interface as the image output interface, and images of 4 megapixel and 16 bit each can be transferred to a computer in 100 frames/s (full frame) without detector memory limitations. The 3D dynamical structures of the air sac at 150 successive time points were obtained after the image reconstruction. Figure 1 shows a photograph of the bell cricket used in the experiments (a) and the 3D reconstructed image of the air sac of the insect (b). The region of interest for the imaging was marked with a red rhombus frame, as shown in (a). The 3D reconstructed image shown in Fig. 1 shows that the compression of the air sac during breathing exhibited obvious anisotropic characteristics, contrary to the hypothesis of isotropy,

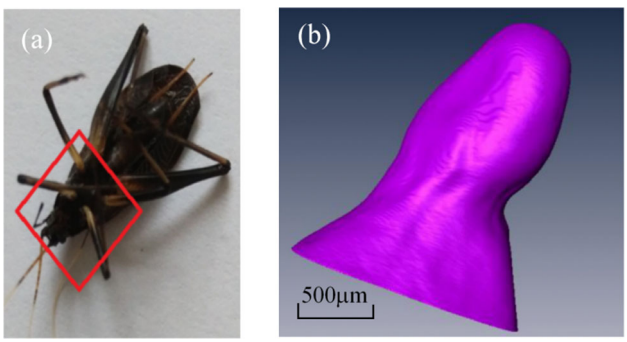

Fig. 1 (Color online) Photograph of bell cricket used in experiments. Region of interest for the imaging is marked with red rhombus frame (**a**) and 3D reconstructed image of air sac (**b**) [2]

thereby providing new knowledge for further research regarding the insect respiratory system.

To further improve the temporal resolution of the X-ray dynamic micro-CT, a fast X-ray imaging detector has been developed at SSRF [4]. An X-ray imaging detector used for white-beam synchrotron radiation is typically based on a scientific high-speed complementary metal-oxide semiconductor (CMOS) camera, a set of long-working distance microscope lenses, and a scintillator screen to realize fast X-ray imaging. However, the coupling efficiency of the long-working-distance microscope lenses is only approximately 5%, thereby limiting the detector efficiency. To increase the coupling efficiency of the lenses, a high-efficiency fast X-ray imaging detector based on a long-working-distance microscope lens system with a large numerical aperture (NA) was developed. The optimized lens system offers an NA of 0.5 at 8 × magnification and four times the coupling efficiency compared with Mitutoyo lenses.

Based on our experimental studies, we discovered that the contrast of images obtained using an indirect X-ray imaging detector based on a coupling lens system can be improved significantly when the thickness of the scintillator is matched with the NA of the lens system [5]. The image qualities obtained using a detector with different scintillator thicknesses of 50, 100, 130, and 200 μm were compared using the JIMA RT RC-02 test pattern (Japan Inspection Instruments Manufacturers' Association, JIMA, Japan). Figure 2 shows the effect of the scintillator thickness on the contrast of images with differently sized feature sizes in the JIMA RT RC-02 test pattern analyzed using a 10 × lens system at 18 keV. The results show that the optimal thickness of the scintillator was 50 μm for the best contrast of the 10 × lens system [5].

Images of sandpaper samples obtained with different scintillator thicknesses of 50, 100, 130, and 200 μm using a 10 × lens system at 18 keV are shown in Fig. 3. Based on the line profiles showing the image contrast obtained with different scintillator thicknesses, we discovered that 50 μm was the optimal scintillator thickness for the best contrast of the 10 × lens system.

Based on the long-working-distance microscope lens system offering an NA of 0.5 at 8 × magnification, a

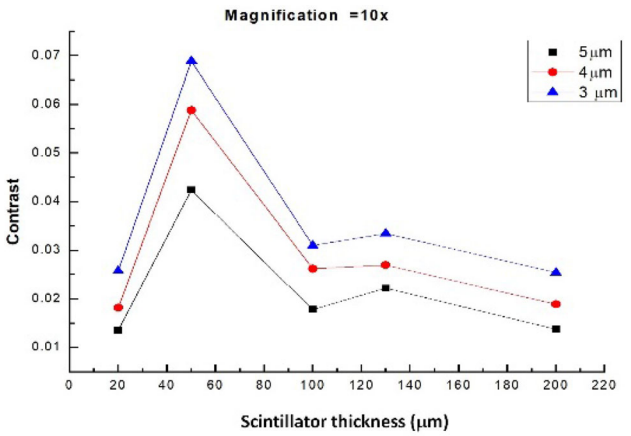

Fig. 2 Effect of scintillator thickness on contrast of images with differently sized feature sizes (3, 4, and 5 μm) in JIMA RT RC-02 test pattern with 10× lens system at 18 keV [5]

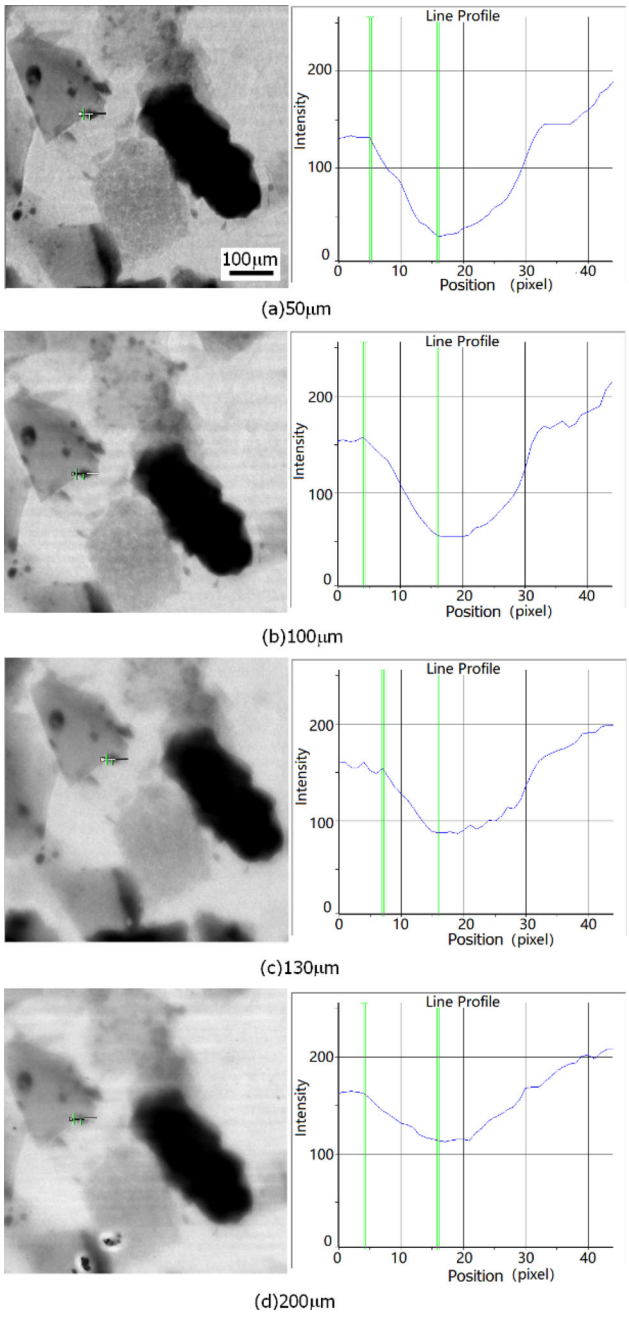

Fig. 3 (Color online) Images of sandpaper samples obtained with different scintillator thicknesses of 50 μm (**a**), 100 μm (**b**), 130 μm (**c**), and 200 μm (**d**) using 10× lens system at 18 keV [5]. Line profiles show image contrast obtained with different scintillator thicknesses using 10× lens system at 18 keV [4]

50-μm-thick LuAG:Ce scintillator and a high-speed visible-light CMOS camera named FastCAM SAZ camera purchased from Photron Co. were used to develop a fast X-ray imaging detector. The pixel size of the camera was 20 μm, the dynamic range was 12 bits, and the memory was 64 GB. For a 1024 × 1024 full pixel resolution, the maximum frame rate was up to 20,000 frames/s. Based on the detector, a dynamic micro-CT experiment with a living ant was performed. The frame rate was 8000 fps, and each set of CT data included 320 projections. The temporal sampling rate was 25 Hz (25 tomograms/s); the effective pixel size was 2.5 μm; the field of view was 1.6 mm × 0.7 mm. Figure 4 shows the reconstructed 3D image series at different times, i.e., 2.24 s (a), 2.40 s (b), 2.48 s (c), 2.56 s (d), 2.65 s (e), and 3.20 s (f), of the moving process of the living ant using dynamic micro-CT. As shown in Fig. 4, the fine structures of the ant body included the abdomen, tail, and four legs are clear. The black ovals signify the positions of the legs after movement.

For fast X-ray imaging and dynamic X-ray micro-CT, a dedicated fast X-ray imaging beamline (BL16U2) based on a cryogenic permanent magnet undulator source is being constructed in the phase-II project of SSRF. The beamline will provide X-ray imaging techniques with various temporal resolutions from milliseconds, microseconds, to 100 ps as well as micrometer spatial resolutions for fast processes, such as high-speed spray processes of fuel, dynamic response processes of materials under dynamic loads, deformations and solidification processes of alloys, and dynamics processes of soft matter systems. The photon energy range is 8.7–30 keV. The beamline construction and commissioning will be completed by mid-2021. Moreover, the BL13W1 beamline is being upgraded. The beamline will involve the use of a super bending magnet source with 2.293 T magnetic field intensity and a double multilayer monochromator, which can provide a white beam with high flux for fast X-ray imaging and dynamic X-ray micro-CT.

2.2 X-ray fluorescence computed tomography (XFCT)

X-ray fluorescence computed tomography (XFCT) can yield the 3D spatial distribution of elements in the sample. XFCT is based on the detection of photons from the fluorescent emission of elements in the sample. A pencil beam of external radiation was used to stimulate the emission of characteristic X-rays in the sample; subsequently, the sample was scanned and rotated through the pencil beam in a first-generation tomographic geometry [6].

An XFCT experiment with 54 keV X rays and 200 μm resolution was performed to obtain the distribution of rare earth elements (REEs) in fish teeth from deep-sea mud. Figure 5 shows the photograph of the fish teeth and the two-dimensional (2D) reconstructed cross-sectional distributions of REEs [7]. The experimental results indicate some coupling relationships between different REEs.

The sample was scanned with a pencil beam in a XFCT experiment, which required a long image acquisition time to acquire a complete set of line integrals step-by-step; therefore, the efficiency was extremely low. To improve the efficiency of the XFCT experiment, a full-field XFCT (FF-XFCT) method [8] was developed to reconstruct the 3D distribution of different elements. Figure 6 shows the sketch of the test sample, a photograph of the prototype full-field XFCT (a), and a photograph of full-field XFCT experimental setup (b). An X-ray CCD (Photonic Science, FDI-VHR) with a pinhole was used to detect the fluorescent photons and was placed 90° from the incident X-ray beam to minimize the scattering photons. Another X-ray CCD camera was used to detect the transmission X-rays for transmission CT. A silicon drift detector was used to verify the presence of different elements in the illuminated area

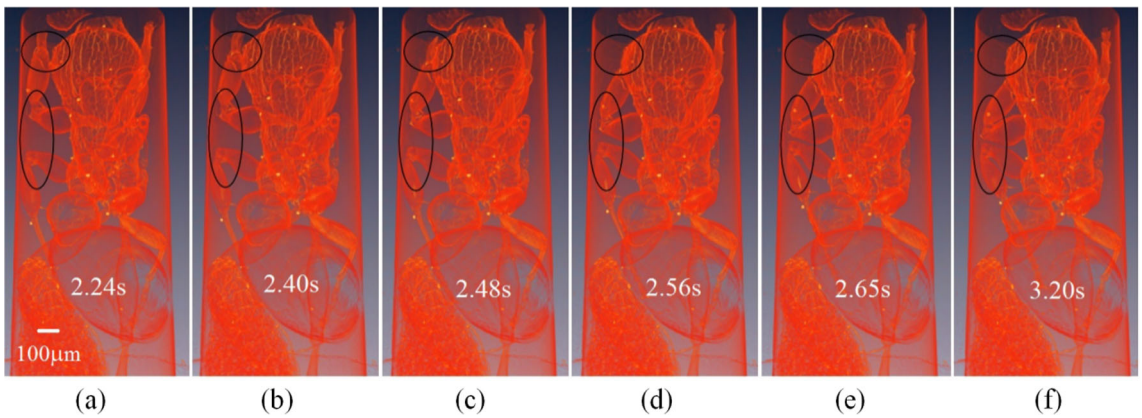

Fig. 4 (Color online) Reconstructed 3D image series at different times, i.e., 2.24 s (**a**), 2.40 s (**b**), 2.48 s (**c**), 2.56 s (**d**), 2.65 s (**e**), and 3.20 s (**f**), of the moving process of a living ant using dynamic micro-CT with a temporal sampling rate of up to 25 Hz (25 tomograms/s) [4]

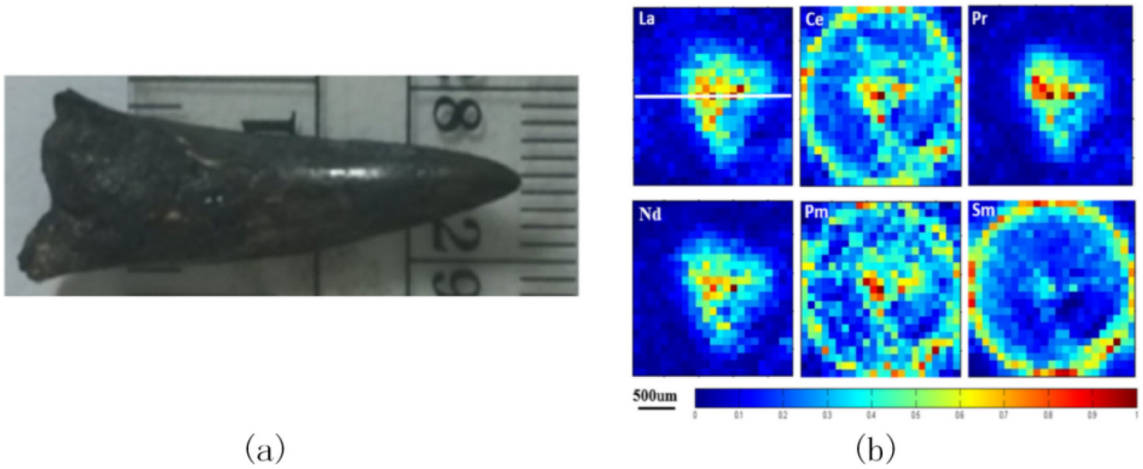

Fig. 5 (Color online) Photograph of fish teeth (**a**) and 2D reconstructed distributions of various REEs in fish teeth (**b**) [7]

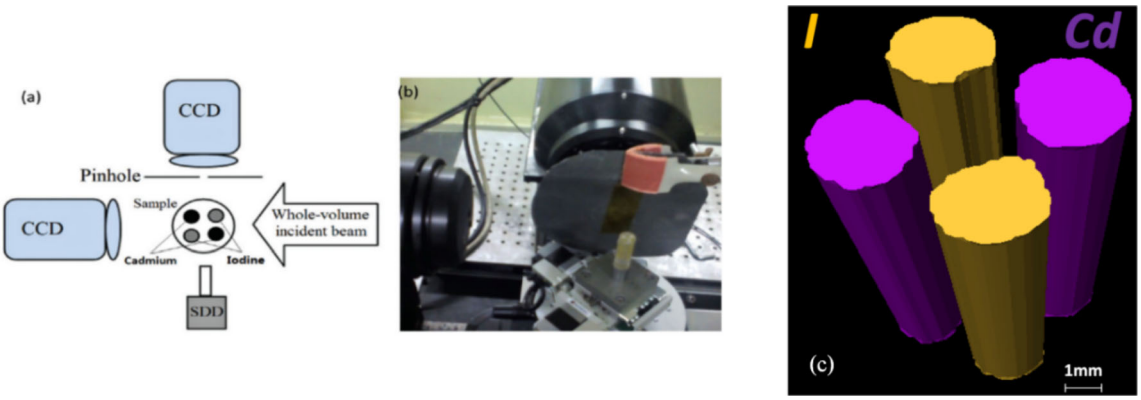

Fig. 6 (Color online) Sketch of test sample and photograph of prototype full-field XFCT (**a**); photograph of full-field XFCT experimental setup (**b**). 3D cadmium and iodine images obtained via FF-XFCT (**c**) [8]

on the sample. A monochromator was used to realize precise energy tuning. Using the FF-XFCT system with image subtraction, 3D elemental distributions can be reconstructed. Figure 6c shows 3D images of cadmium and iodine obtained via FF-XFCT. The experimental results shown in Fig. 6 indicate that FF-XFCT is a simple yet highly efficient approach for effective 3D element imaging.

2.3 3DXRD

The 3DXRD method was used to identify grains in heterogeneous polycrystalline materials, providing information on locations, sizes, shapes, crystal orientations, and elastic deformations. In addition, during deformation or annealing, grains can be analyzed in situ. Figure 7 shows a schematic diagram of the experimental setup. By recording the diffraction pattern at two distances using a near-field and far-field detector, a straight line can be extrapolated through the corresponding diffraction spots at different

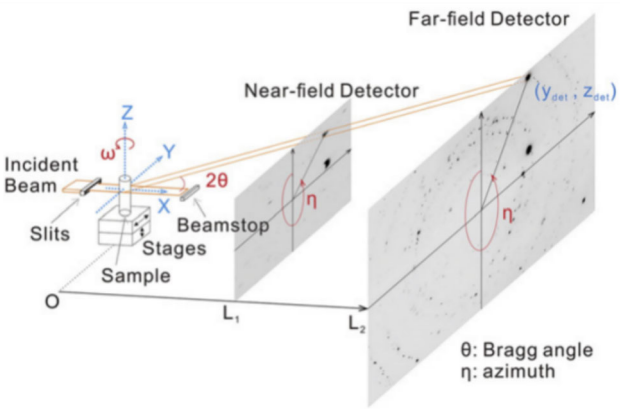

Fig. 7 Schematic diagram of experimental setup of 3DXRD

distances until the sample to determine the position of the diffracting volume element [9].

Minor phases in metals and alloys significantly affect their mechanical and physical properties. Using conventional metallographic methods, it is difficult to be

determine unknown minor phases in polycrystalline materials. Hence, a 3DXRD-based method was developed. By merging the frames collected during a full 360° rotation, the single-crystal-quality pseudo-powder diffraction pattern of an unknown minor phase can be extracted from 3DXRD data. Subsequently, the unit cell and probable cell symmetry can be determined using relatively straightforward methods derived from the standard powder diffraction methodology. Once the unit cell of an unknown minor phase is determined, then standard 3DXRD analysis can be performed.

The commercial aluminum alloy AA6061 was used as the test sample. Experiments were performed on the BL13W1 beamline at SSRF. Figure 8 shows the (2θ, η) plot of the searched peaks obtained by merging the far-field ω frames at a high (a) and low threshold level (b). The inset in (b) shows the solution for the unknown minor phase, which is consistent with γ-Fe (austenite) phase. Figure 9 shows the 3D crystal grain reconstructions of the Al (a) and γ-Fe phases (b) via the 3DXRD method. The experimental results show that the crystal grains of an unexpected γ-Fe phase appeared only on the surface of the bulk sample of aluminum alloy AA6061, and that the γ-Fe phase might be generated during sample preparation [10]. Therefore, we conclude that the 3DXRD method is effective for the identification of unknown minor phases in bulk alloys of various crystal systems.

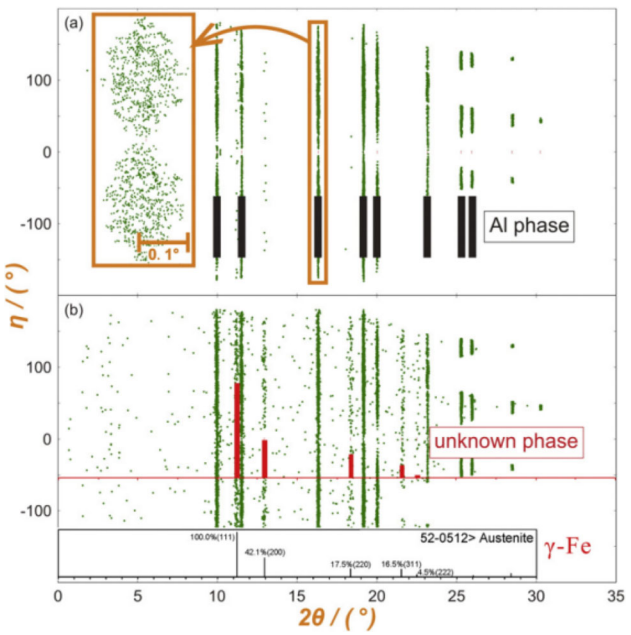

Fig. 8 (Color online) (2θ, η) plot of searched peaks obtained by merging far-field ω frames at high threshold level (**a**) and low threshold level (**b**) [10]

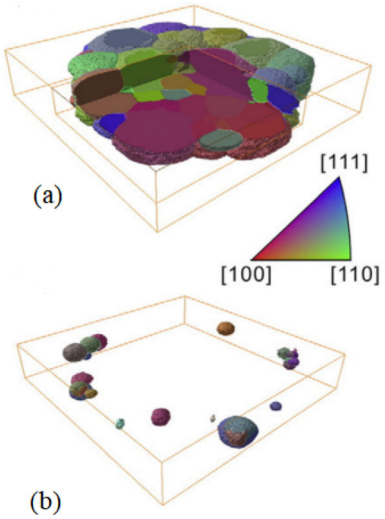

Fig. 9 (Color online) 3D crystal grains reconstructions of Al (**a**) and γ-Fe phases (**b**) [10]

2.4 SAXS-CT

Combined with SAXS and CT, SAXS-CT can reconstruct the reciprocal space information of each position in the sample. It is a nondestructive analysis method for the nanostructure of inhomogeneous materials. The schematic diagram of SAXS-CT is shown in Fig. 10a. A pencil beam is incident on the sample to generate the scattering pattern, which is recorded using a 2D detector. Figure 10b shows the scanning strategy for data acquisition. The 2D SAXS patterns are collected point by point by translating the sample along the u-axis and then rotating around the z-axis at a constant angular interval $\Delta\phi$. The procedure is repeated until the sample is rotated by 180°. For a new slice, all of the abovementioned procedures are repeated once more. To obtain the 3D information of the sample, a large number of slices is typically required, implying that the data acquisition process of SAXS-CT is time-consuming. Figure 10c shows the data-processing procedure for SAXS-CT. SAXS-CT cannot be used as a general experimental method for synchrotron radiation applications because of its long acquisition time for large data. To reduce the acquisition time of SAXS-CT data, the ordered subset expectation maximization (OSEM) algorithm was used in the reconstruction. The OSEM algorithm is more accurate than the filtered backprojection algorithm, and it can efficiently suppress the deterioration of image quality within a large range of angular sampling intervals. The proposed method was validated using limited projection data in an experiment on a bamboo sample [11].

For the design and manufacture of high-performance polymeric products, it is critical to investigate the evolution of the hierarchical crystalline structure in the injection-molded polymer and then understand the process–structure

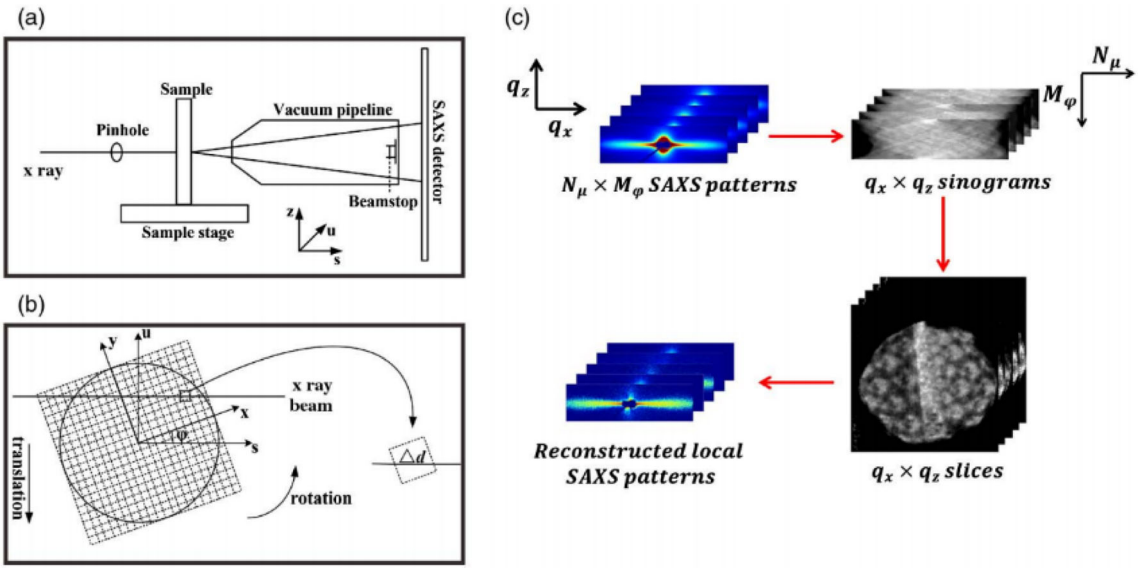

Fig. 10 (Color online) **a** Side view of schematic diagram of SAXS-CT. Scattering pattern from pencil beam recorded using a 2D detector; **b** scanning strategy for data acquisition, where *d* represents intersection length of the ray with the pixel; **c** data-processing procedure for SAXS-CT [11]

relationship more comprehensively. SAXS-CT was developed to reveal the 3D distribution and evolution of the hierarchical crystalline structure of injection-molded polylactide (PLA). In this regard, experiments were performed on the BL19U2 beamline at SSRF [12]. The PLA samples were denoted as PLAX, where X represents the shear duration (s). For each injection-molding cycle (the reciprocal movement of the two pistons only for one time), the shear duration was 6 s. The PLA30 part with a medium shear duration was selected, and 60 slices with a step of 100 μm were collected and reconstructed via SAXS-CT. The separated volume element size in the reconstructed SAXS-CT maps was 30 μm × 30 μm × 50 μm. The 3D distribution maps of the shish-kebab structure and the morphological parameters for the PLA30 part were obtained after the reconstruction. Figure 11 shows the 3D distributions of the integrated scattering intensity of the lamella (I_{lamella}) (a), crystal thickness (L_c) (b), long period (L_p) (c), and bulk percentage crystallinity (ϕ_c) (d). The 3D distribution of the morphological parameters in Fig. 11 does not exhibit apparent variations along the flow direction, implying that good uniformity was achieved through injection molding. The experimental results indicate that SAXS-CT is highly effective for establishing the relationship between the inner structure and the process technology of the injection-molded polymer.

2.5 Full-field transmission X-ray microscopy (TXM) and nano-CT

Full-field transmission X-ray microscopy (TXM) and nano-CT enable nondestructive high-spatial-resolution 2D and 3D imaging; they are widely used in morphological and structural studies in various fields. TXM operates based on the same principle of a visible light microscopy. A condenser focuses an X-ray beam to illuminate a sample. Subsequently, a zone plate is used as an object lens, which magnifies the sample image to the detector. Full-field X-ray nano-CT enables nondestructive high-spatial-resolution 3D imaging. In the traditional tomography reconstruction, a large number of projections is required to reconstruct a 3D object; consequently, the acquisition time is long.

Hence, an X-ray nano-CT system based on equally sloped tomography (EST) was established on the BL13W1 beamline at SSRF. Figure 12a, b shows the 2D images of the Siemens star with a 100 nm resolution using a high-resolution zone plate, high-quality condenser, and high-efficiency detector [13]. Figure 12c shows the 3D image of nickel powder (with the average diameter of 1 μm); the experimental results indicate that based on EST technology, 3D tomographic images can be obtained under a low flux density [14]. This technology improves the X-ray nanometer imaging ability of SSRF and can be applied in many fields, such as nanomaterials, new energy, and life sciences.

The BL18B beamline with a photon energy range of 5–14 keV based on a bending magnet is being constructed in the phase II project of SSRF; the goal is to visualize the

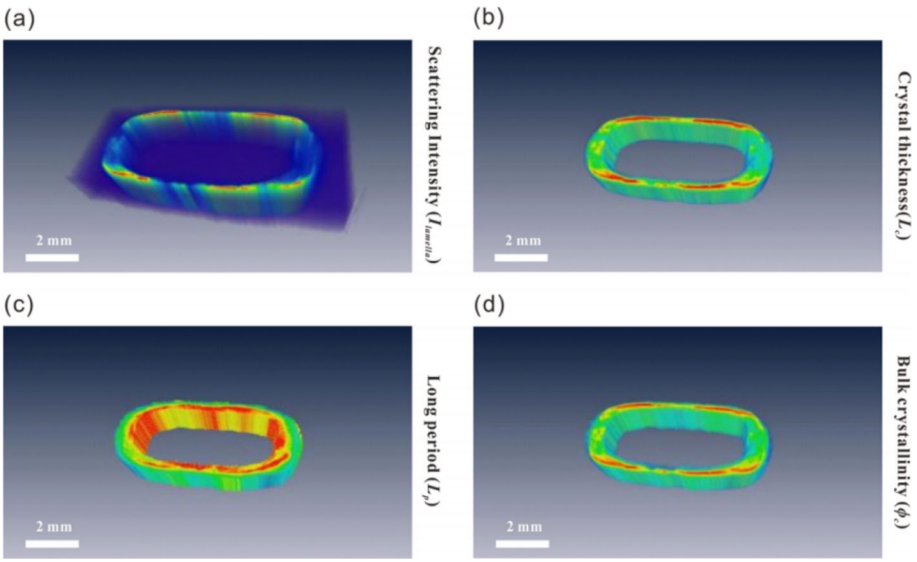

Fig. 11 (Color online) 3D distribution maps of shish-kebab structure, and morphological parameters for PLA30 part. **a** Integrated scattering intensity of lamella ($I_{lamella}$); **b** crystal thickness (L_c); **c** long period (L_p); **d** bulk percentage crystallinity (ϕ_c) [12]

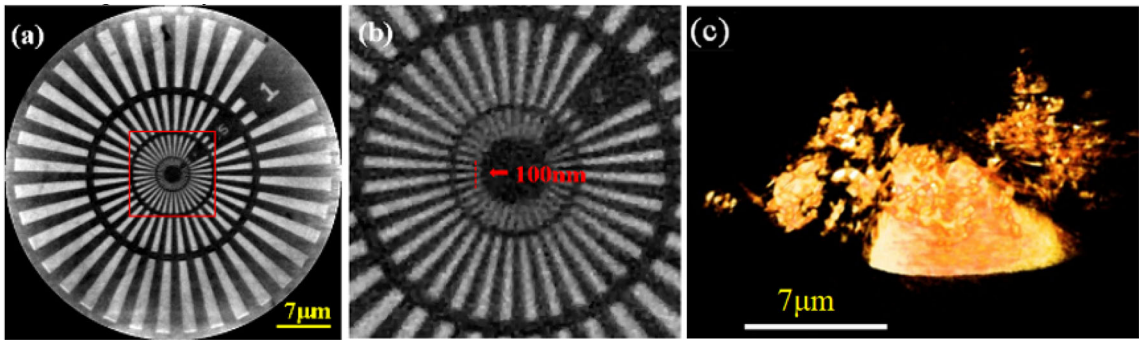

Fig. 12 (Color online) Experimental results: **a** 2D image of Siemens star with 100 nm resolution; **b** amplified image in **a**; **c** 3D image of nickel powder (with average diameter of 1 μm) [14]

nanoscale internal structure in three dimensions. Design goals with the highest spatial resolution of 20–30 nm were proposed at 8 keV. The beamline and TXM end-station construction as well as commissioning will be completed by mid-2021.

2.6 Move contrast X-ray imaging

A contrast agent is typically used to improve the image contrast for the in vivo X-ray imaging of vessels and angiomatous tissue. In traditional X-ray imaging methods, because of intermittent flows, short circulation times of contrast agents in vessels, and nonrigid motions of adjacent tissues, it is extremely difficult to obtain high-quality images of microvessels in vivo. The move contrast X-ray imaging (MCXI) method was developed to overcome the abovementioned problem [15]. The principle of MCXI is to differentiate the migration of contrast agents along vessels from the movement of other tissues by analyzing the frequency of intensity variation at each pixel of the image frame and then visualizing them independently.

Experiments were performed on the BL13W beamline at SSRF, as shown in Fig. 13. Live mice were used as animal models to verify the proposed MCXI. During an MCXI experiment, 180 μL of iodine was injected into internal carotid arteries at an injecting rate of 133.3 μL/s. A PCO X-ray CCD camera (pixel size of 6.5 μm × 6.5 μm; field of view of 13 mm × 13 mm) was placed 65 cm away from the sample. The image sequence was recorded at a frame rate of 100 frames/s with an exposure time of 10 ms for per-frame images. Using the reconstructed images of the dynamic signal of the entire perfusion process, MCXI can realize the complete imaging of the trajectories of contrast agents in blood vessels. Figure 14 shows the experimental results of intact vasculature imaging via MCXI, including the entire vasculature (a), arteries (b), a capillary image with insufficient resolution (c), and veins (d) [15]. The scale bar represents 500 μm. The experimental results show that the method successfully realized the separate imaging of the arterial vascular system and venous vascular system in vivo to eliminate the mutual interference of different microvascular systems. The ability of MCXI in

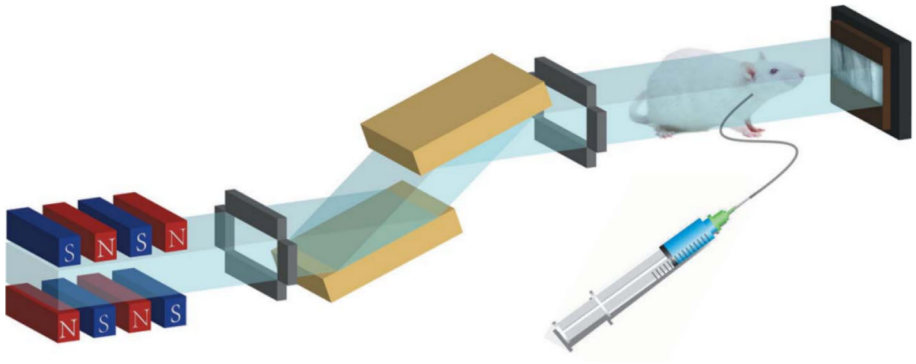

Fig. 13 (Color online) Experimental setup for MCXI with synchrotron X-rays [15]

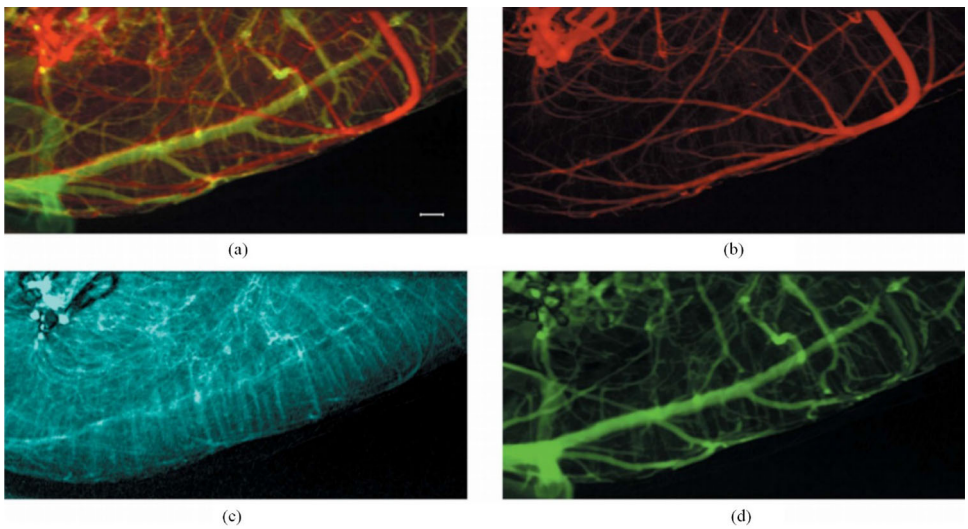

Fig. 14 (Color online) Intact vasculature imaging with MCXI, including the entire vasculature (**a**), arteries (**b**), a capillary image with insufficient resolution (**c**), and veins (**d**). Scale bar represents 500 μm [15]

reconstructing the complete perfusion process of contrast agents may be exploited to investigate hemodynamics in certain vessel segments.

2.7 X-ray speckle-tracking imaging

Based on tracking near-field speckles, X-ray speckle-tracking imaging can be used to measure the first derivative of the phase. This method can not only detect the phase gradient information of the sample, but can also detect the 2D absorption and scattering information of the sample using a 2D detector and a random phase sample. Additionally, it can be performed well using laboratory X-ray sources and in synchrotron facilities. However, the application of speckle-tracking imaging is limited by the edge enhancement effect. Hence, an image reconstruction method using an additional in-line phase-contrast image is proposed as the speckle image is inevitably modulated by a propagation-based phase-contrast image. The sample-and-speckle image $I_{\text{distortion}}$ and the sample-only image $I_{\text{transmission}}$ were recorded under the same conditions. Subsequently, $I_{\text{transmission}}$ was employed to normalize $I_{\text{distortion}}$ to deconvolve the propagation-based phase-contrast image from the speckle image. To demonstrate the practicability of this method, experiments were performed on the BL13W1 beamline at SSRF. A biological sample of a scorpion's claw was used to verify the proposed speckle-tracking method. Figure 15 shows the in-line phase-contrast image of a scorpion's front claw (a), as well as the phase images of a scorpion's front claw using normal speckle-tracking (b) and the proposed method (c) [16]. The experimental results shown in Fig. 15 indicate that the proposed method effectively eliminated the effects of edge enhancement. Hence, this method enables the applications of the speckle-tracking method in material and biomedical samples to be expanded.

3 Applications

Experimental results of typical applications on the BL13W1 beamline will be introduced in this section.

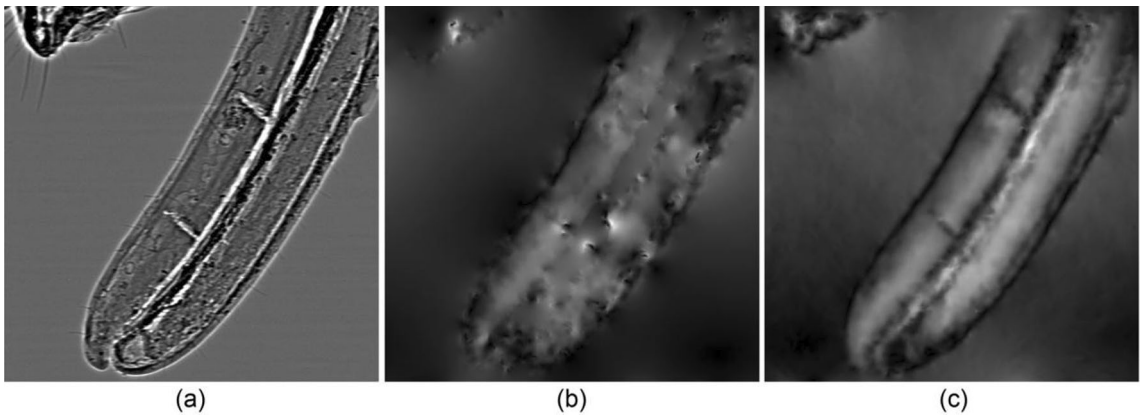

Fig. 15 **a** In-line phase-contrast image of scorpion's front claw; phase images of scorpion's front claw using **b** normal speckle-tracking and **c** proposed method [16]

3.1 Materials science

The beamline can provide a high spatial resolution of 0.325 μm/pixel for X-ray micro-CT. Superhydrophobicity in nature has inspired researchers to develop artificial surfaces with desirable wetting properties for various applications. The surfaces of artificial superhydrophobic carbon nanotube films were nondestructively analyzed with this pixel size in three dimensions using synchrotron radiation X-ray micro-computed tomography (SR-μCT). Figure 16a shows the schematic illustration of SR-μCT for observing a solid–liquid–vapor (SLV) interface on a MWNTs/Nafion film. Figure 16b shows that the extraction of air and water phases (purple for air, blue for water) was implemented within a selected region (marked in the red box in c) near the surface shown in Fig. 16c. The reconstructed images of the SLV distribution surrounding the surfaces in Fig. 16 show that the protruding structures were crucial for the superhydrophobicity because they trapped a layer of air up to 14 μm thick [17].

In biological materials, SR-μCT with a spatial resolution of 9 μm/pixel is suitable for observing the porous structures of bones. To evaluate the regenerative treatment effect of osseous defects, SR-μCT imaging was performed to investigate the effects of different scaffolds in vivo, such as bioinspired trimodal porous scaffolds loading rhBMP-2 [18], PEGylated poly-modified calcium phosphate scaffolds [19], MBG-modified β-TCP scaffolds [20], and MBG scaffolds containing chitosan microspheres [21].

Figure 17 shows the 3D visualized morphology of cracks of multilayer composite materials during an in situ tensile test at various macro-strains: (a) 0%; (b) 3.0%; (c) 5.0%; (d) 10.0%; (e) 20.0%. As shown in Fig. 17, SR-μCT effectively tracked the strain evolution process and crack growth of multilayer composite materials. It has been used to analyze the effect of hierarchical structure on deformation/crack behaviors as well as investigate microstructural heterogeneity design to alleviate cracking tendency and strain localization [22, 23].

To evaluate the reliability of a through-silicon via (TSV), it is vital to obtain precise 3D morphological

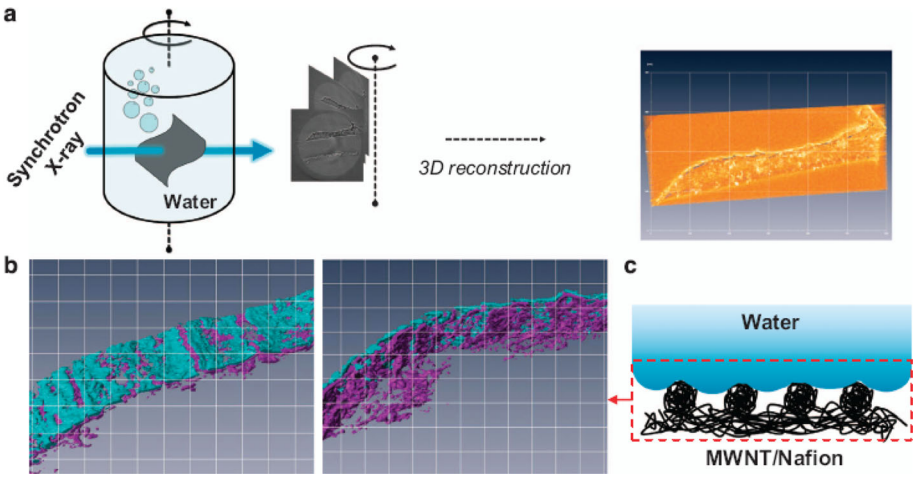

Fig. 16 (Color online) **a** Schematic illustration of SR-μCT for observing SLV interface on MWNTs/Nafion film. Subregion (marked in red box in c) near the surface was selected for analysis. Grid has a scale of 100 μm, **b** air (purple) and water (blue) phases were extracted, highlighted, and viewed from different angles. Grid has a scale of 25 μm, **c** schematic of SLV interface on the film [17]

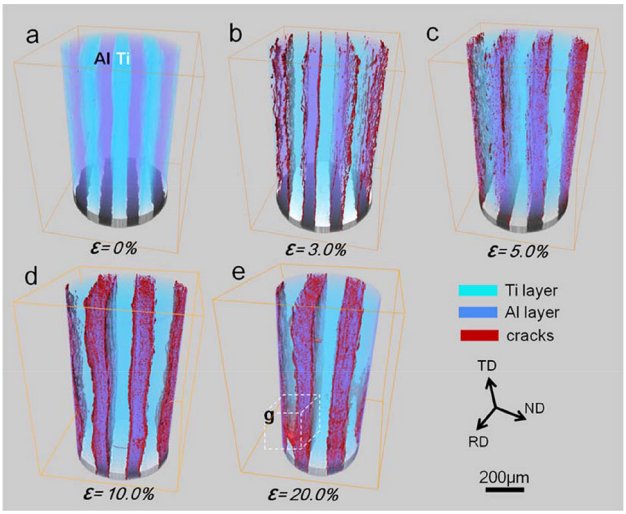

Fig. 17 (Color online) 3D visualized morphology of cracks of multilayer composite materials during n situ tensile test at various macro-strains: **a** 0%; **b** 3.0%; **c** 5.0%; **d** 10.0%; **e** 20.0% [23]

descriptions and statistical features of via formation based on the Bosch process. A highly sensitive phase-contrast X-ray micro-CT method based on the recorrection of abnormal projections was presented by the X-ray imaging group at SSRF to provide a comprehensive and quantitative characterization of TSV etching performance. By replacing abnormal projections at specific angles with neighboring projections according to linear interpolation principles, the interface between silicon and air can be distinguished using phase-retrieval algorithms. Figure 18 shows the reconstructed 3D microstructures of the TSV etching, in which the blue part represents the silicon base, whereas cylinders rendered by multiple colors represent vias [24]. The reconstructed 3D microstructures can be applied directly to a reference and model for further finite element analysis.

Owing to the high-energy X-rays of the BL13W1 beamline and the imaging plate detector, high-energy X-ray diffraction (XRD) patterns can be obtained with a wide q range. To clarify the role of minor Y and Nb additions in $Fe_{72}Y_6B_{22}$ and $Fe_{68}Nb_4Y_6B_{22}$ using the pair distribution function (PDF), experimental data from synchrotron XRD with energy of 69.5 keV and an extended X-ray absorption fine structure were combined with reverse Monte Carlo simulations to construct 3D atomic packing for Fe-based metallic glasses. Figure 19 shows the structural factor $S(q)$ and pair correlation function $g(r)$ (inset) obtained by XRD. The results show that the addition of Y and Nb atoms mainly replaces the center Fe atoms, stabilizes large high-coordinated polyhedra, and promotes the formation of icosahedron-like clusters and their connectivity with high-coordinated polyhedra [25].

3.2 Biomedicine

Synchrotron radiation X-ray absorption contrast imaging is typically used in vascular angiography by in vivo dynamic imaging and 3D imaging of vascular microstructures by micro-CT. Multiple modality dynamic imaging methods were applied to observe the structure and function of collateral circulation in vivo. Synchrotron radiation imaging was applied to observe small blood vessels of tens of microns and their dynamic changes. Through in vivo X-ray dynamic imaging, the effect of rapamycin on the therapy of middle cerebral artery occlusion (MCAO) was evaluated. The experimental results shown in Fig. 20 show that the rapamycin can improve the blood supply in the middle cerebral artery region after MCAO. These technologies enabled the calculation and investigation of functional changes, such as cerebrovascular elasticity and vascular volume changes. It has been proven that collateral vessels exist in the bottom, deep, and surface of the brain during cerebral ischemia, and that collateral circulation can be regulated using drugs. This research not only provided a unique method for the experimental research of cerebral ischemia, but also maintained China's international leadership in the research of micro-blood vessels [26].

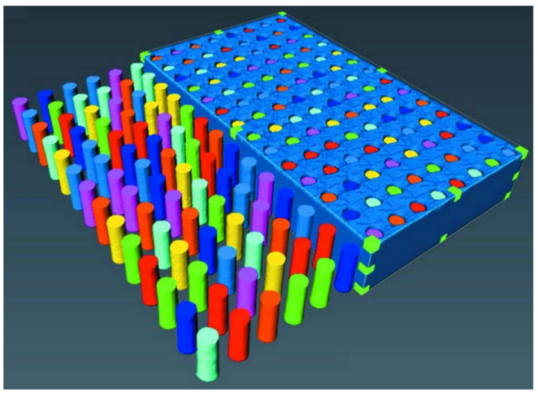

Fig. 18 (Color online) 3D visualization of TSV etching [24]. Different colors used to distinguish vias from one another

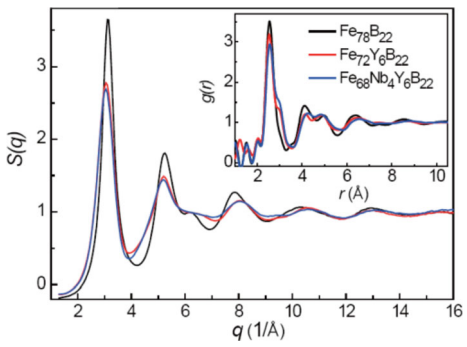

Fig. 19 (Color online) Structural factor $S(q)$ and pair correlation function $g(r)$ (inset) of $Fe_{78}B_{22}$, $Fe_{72}Y_6B_{22}$ and $Fe_{68}Nb_4Y_6B_{22}$ obtained by XRD [25]

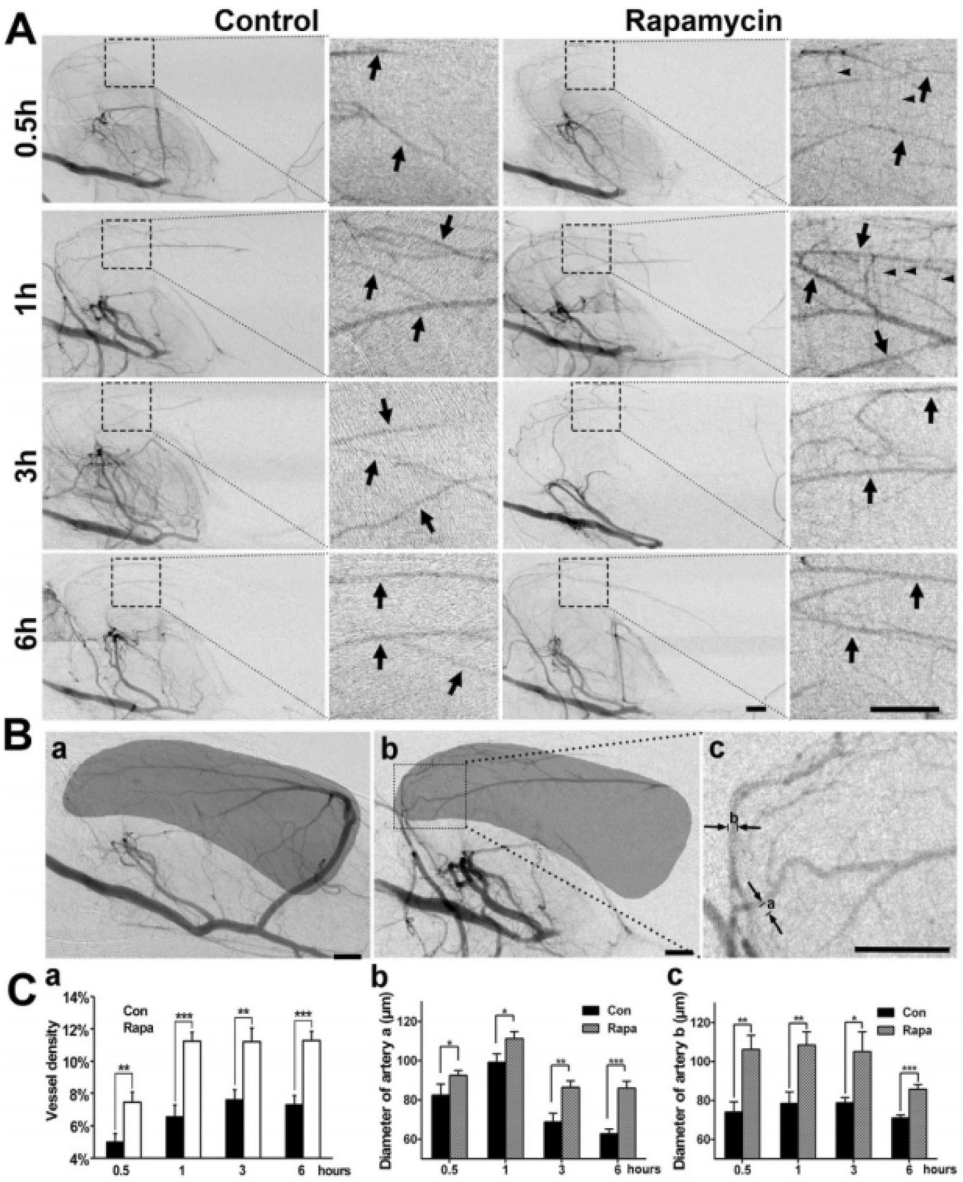

Fig. 20 SR angiography shows that rapamycin improves blood supply to middle cerebral artery (MCA) [26]. (A) Dynamic SR angiography showing changes in posterior cerebral artery (PCA) blood flow and its branches at 0.5, 1, 3 and 6 h of MCAO in rapamycin-treated and MCAO-alone rats. Arrows indicate enlarged view of PCA branches, and that these branches reach toward the MCA territory after MCAO. Small arrowheads indicate cortical penetrating artery. Scale bar: 1 mm, (B) SR angiography showing MCA territory in normal (**a**) and MCAO rats (**b**). Shadowed areas illustrate region of microvessel selected for measuring microvessel density. In **c**, diameters a and b indicate two main collateral arteries from PCA toward MCA during MCAO. (C) Bar graph showing microvessel density (**a**), diameter of collateral *a* (**b**), and diameter of collateral *b* (**c**) after 0.5, 1, 3 and 6 h of MCAO in rapamycin-treated and MCAO-alone rats. Scale bar: 1 mm; $n = 6$ per group; $*p < 0.05$; $**p < 0.01$; $***p < 0.001$; rapamycin-treated versus control rats

The SR-μCT of the absorption contrast was performed to reconstruct the 3D microvasculature of the spinal cord before and after spinal cord injury. Subsequently, the vascular volume information in the injury area was analyzed. Figure 21 shows the 3D microvasculature of the spinal cord at the T10 level in UTXf/f and UTX −/− mice at 28 days post-sham or spinal cord injury surgery, and the quantification of the vessel volume fraction. As shown, a new mechanism of ubiquitously transcribed tetratricopeptide repeated on chromosome X (UTX), thereby epigenetically promoting vascular regeneration and functional recovery post-spinal cord injury. The results are expected to provide a new target for the treatment of spinal cord injury [27].

The quantitative analysis of microvasculature is crucial for the angiogenesis analysis of liver fibrosis or tumor growth. The statistical characteristics of microvasculars can be extracted from microvascular skeletons through skeletonization. In medical research, thinning is a typically used algorithm for forming the vascular skeleton. The precision of the quantitative results of vascular geometric parameters, such as the counts of vessel segments, branching points, and vascular length, is limited in the existing 3D thinning methods. A new thinning method has been proposed by the X-ray imaging group at SSRF. By detecting the end-points of terminal branches in a vessel tree before thinning begins, the detected endpoints located at the boundary of an object were used as constraints for the extraction of the skeleton. This method can maintain the topological and geometric structure of blood vessels simultaneously. The entire hepatic vein of a rat and the skeletons generated based on our proposed method are

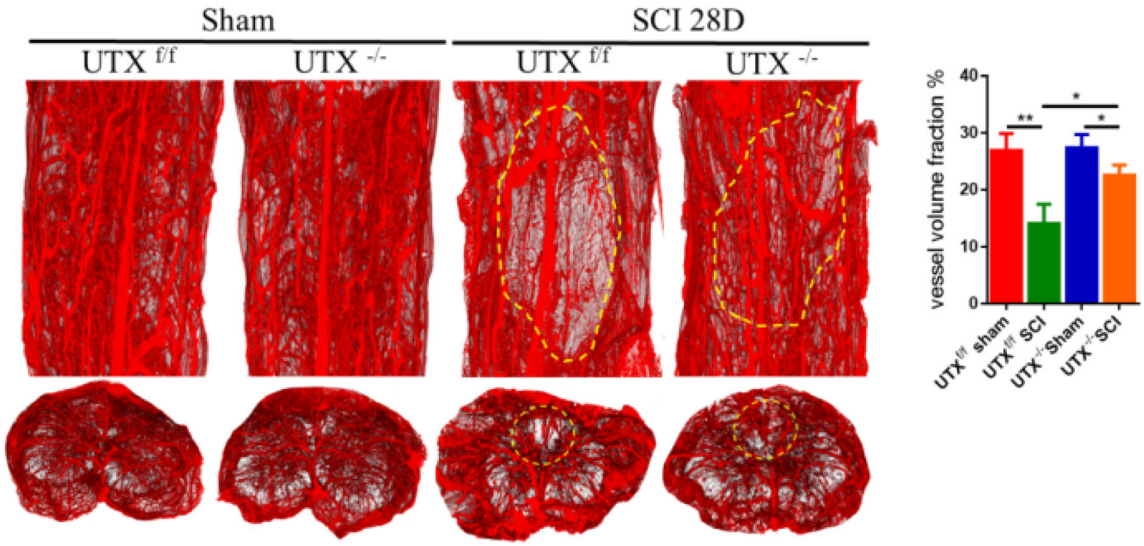

Fig. 21 (Color online) 3D microvasculature of spinal cord at T10 level in UTXf/f and UTX-/- mice at 28 days post-sham or spinal cord injury surgery, and quantification of vessel volume fraction [27]

shown in Fig. 22. Experimental results indicate that the skeletons generated based on the proposed method can significantly improve the precision of the skeleton and enable a more precise quantitative analysis of vascular structures for assessing anti-angiogenesis treatments and the early detection of tumors [28].

In pharmacology, the multistructural information of a tablet on the internal matrix layer, protective cushion layer, and pellets is obtained based on SR-μCT. Figure 23 shows the 3D structure of a tablet and its material distributions in slices. In this study, the relationship between the spatial distribution of active components and excipients and the microstructure of the multi-unit particle system tablets was analyzed in depth, which facilitates the quantitative model design of drug delivery systems. Regional chemical measurement based on microstructure characterization is a new method for the quality evaluation and development of drug delivery systems [29].

3.3 Paleontology

In paleontology, noninvasive characterization of the inner structure of valuable samples in three dimensions is important. In 2016, scientists discovered the first bird

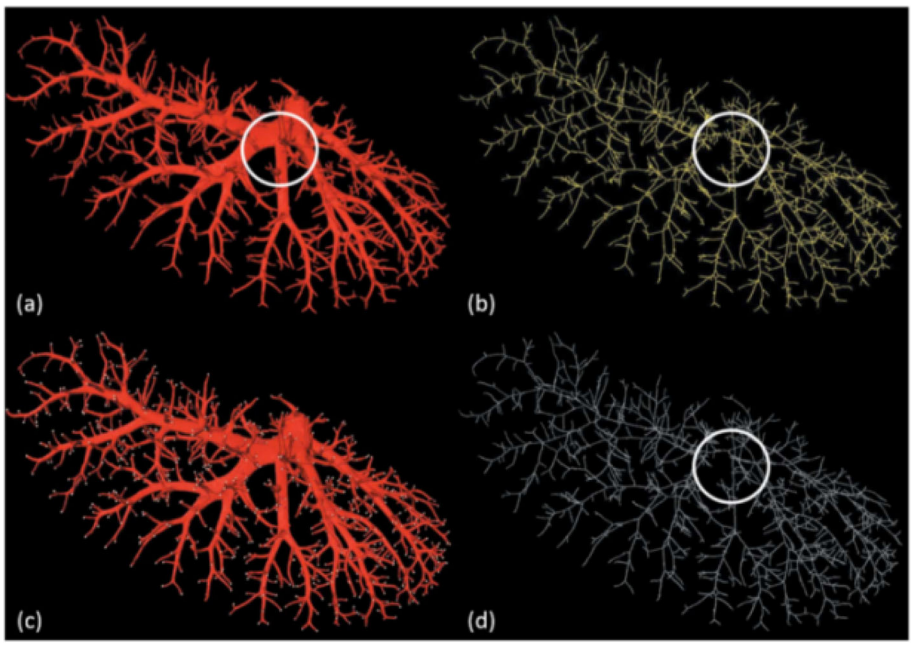

Fig. 22 (Color online) **a** Image of entire vascular structure of rat hepatic vein, **b** skeleton extracted based on ITK 3D thinning filter, **c** extracted end-points, **d** skeleton extracted using our method [28]

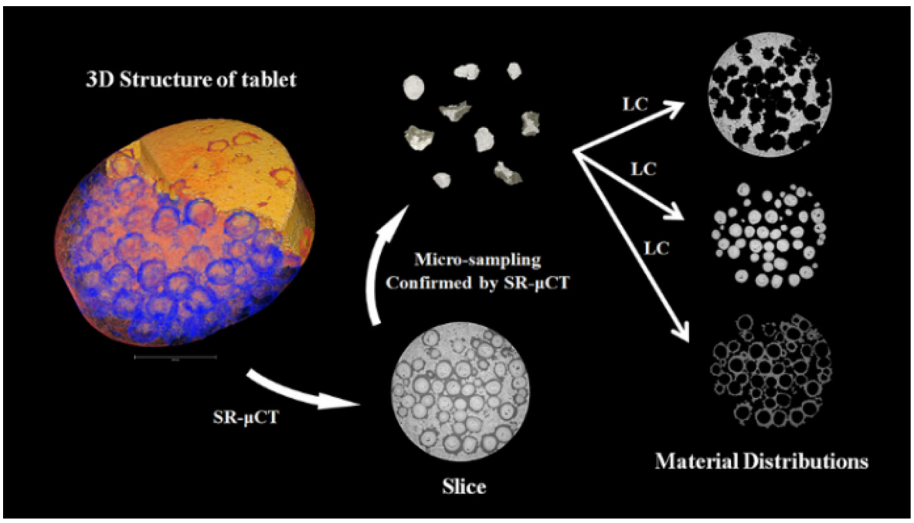

Fig. 23 (Color online) 3D structure of tablet and material distributions in slices [29]

specimens in amber; 99 million-year-old bird wings were fossilized in Burmese ambers. Prior to this, knowledge of Cretaceous birds was limited to fossil records and served as the first glimpse into ancient birds from the age of dinosaurs. Using nondestructive SR-CT technology, the 3D morphologies of the outer skin (including the feather trunk) and the inner bone of the wing in the amber sample were reconstructed. Figure 24 shows the amber sample and SR X-ray CT reconstructions of osteology. Based on the 3D shape of the reconstructed bone, the specimen was determined to be Enantiornithes [30].

Scientists reported the discovery of a juvenile toothed and an adult toothless dinosaur in Xinjiang, i.e., the first time that the teeth were found missing in a dinosaur. This provides important clues to the evolution of bird beaks [31]. This dinosaur, which gradually lost its teeth during individual development, is known as the Limusaurus and was discovered in the Wucai Bay area of the Xinjiang region. The team continued to use the BL13W1 beamline and discovered that the gradual loss of teeth during individual development was also present in the Oviraptor and the Early Cretaceous bird Sapeornis; furthermore, they discovered that tooth loss occurred earlier in the evolution of dinosaurs compared with birds, suggesting that the heterotopic degeneration of teeth is the direct cause of tooth loss in birds [32]. Figure 25 shows the jaw bones of the Limusaurus illustrated via CT imaging and diagrammed tooth-loss patterns.

3.4 Physics

In physics, intensity correlated imaging, also known as ghost imaging, is an emerging technology based on the intensity fluctuation characteristic of light. It can nonlocally acquire the information of a sample by measuring the second-order intensity correlation between the reference

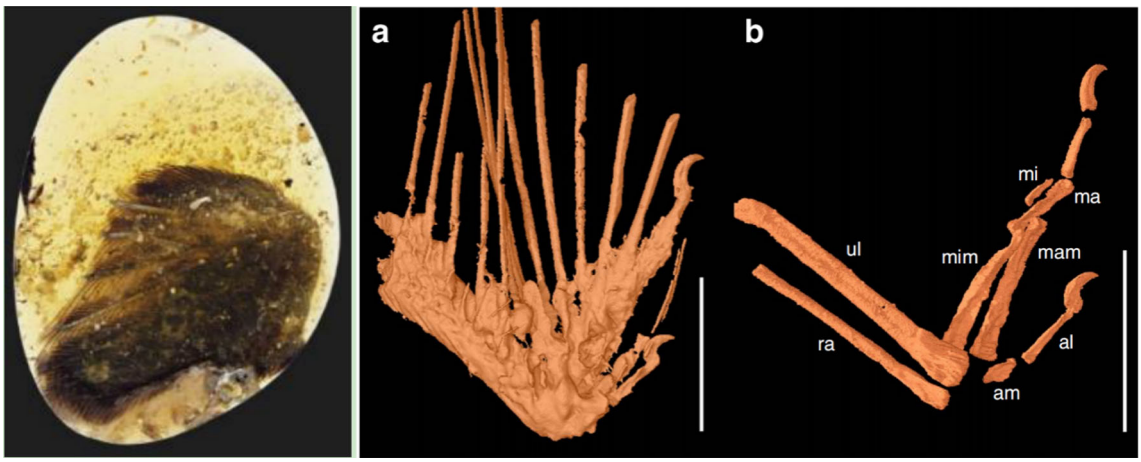

Fig. 24 (Color online) Photograph of amber sample (left figure) and SR X-ray CT reconstructions of sample osteology (right figure: **a**) [30]. Skeletal morphology of sample osteology using different density thresholds (right figure: **b**). al, alular digit; am, alular metacarpal; ma, major digit; mam, major metacarpal; mi, minor digit; mim, minor metacarpal; ra, radius; ul, ulna. Scale bar, 5 mm

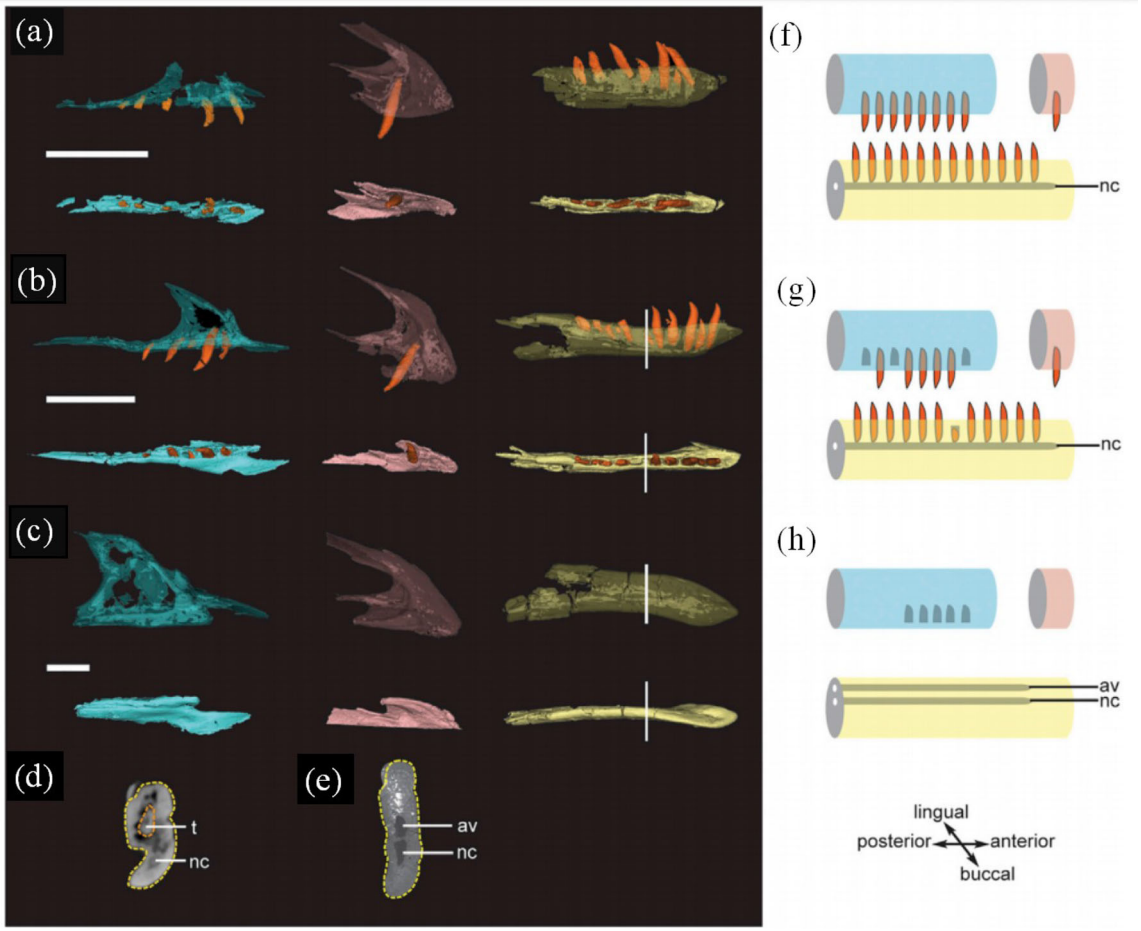

Fig. 25 (Color online) Jaw bones of L. inextricabilis illustrated by CT data, and diagrammed tooth-loss pattern in *Limusaurus inextricabilis* [31]. **a–e** Jaw bones of *L. inextricabilis*: premaxilla (right), maxilla (middle), and dentary (left) of stage I Limusaurus (Sample a), stage II Limusaurus (Sample b), and stage IV Limusaurus (Sample c) in right lateral and ventral views; transverse view of middle portion of dentary of stage II Limusaurus (**d**), and stage IV Limusaurus (**e**). av, alveolar vestiges; nc, neurovascular canal; t, tooth. (f)–(h) Diagrammed tooth-loss pattern in L. inextricabilis. Scale bars in **a–c** represent 1 cm. Bars in **d–h** are not to scale

and the test optical fields. In 2016, scientists demonstrated the hard X-ray Fourier transform ghost imaging (FGI) method and obtained the X-ray Fourier-transform diffraction patterns of a noncrystalline sample by measuring the intensity correlation in the Fresnel zone; subsequently, they successfully reconstructed the sample's amplitude and phase distributions. Figure 26 shows the Fourier-transform diffraction pattern of the experimental sample and distributions in the spatial domain retrieved (top: amplitude distribution, bottom: phase distribution) [33]. A spatially incoherent pseudothermal X-ray source with a 0.1 nm wavelength was adopted in the experiment. It was the first demonstration of Fourier-transform X-ray ghost imaging.

Under mechanical loads, granular materials yield plastic deformation, which is crucial for the construction of macrostructure models and the understanding of shear band formation. However, for disordered granular materials, the microscopic nature of plastic deformation is unclear. The 3D structural changes of granular materials under shear were in situ analyzed using X-ray tomography based on synchrotron radiation. Figure 27 shows the schematic of the plane shear cell (a), absolute z-displacement of each particle after the first shear step and the steady states, respectively (b, c), and carrier of plasticity (d) in amorphous materials [34]. It was demonstrated that similar to a 2D neighborhood exchange event, a 3D basic plastic event is a reversal event composed of two pairs of particles exchanging neighborhood with each other in a highly deformed coplanar tetrahedron on the Delany network. Therefore, in disordered granular packing, the highly deformed coplanar tetrahedron, as the plastic dislocation-like structural carrier, will induce plastic deformation during the inversion process.

3.5 Chemistry

Metal electrodeposition is an important process in resource recovery, anti-corrosion coatings, and

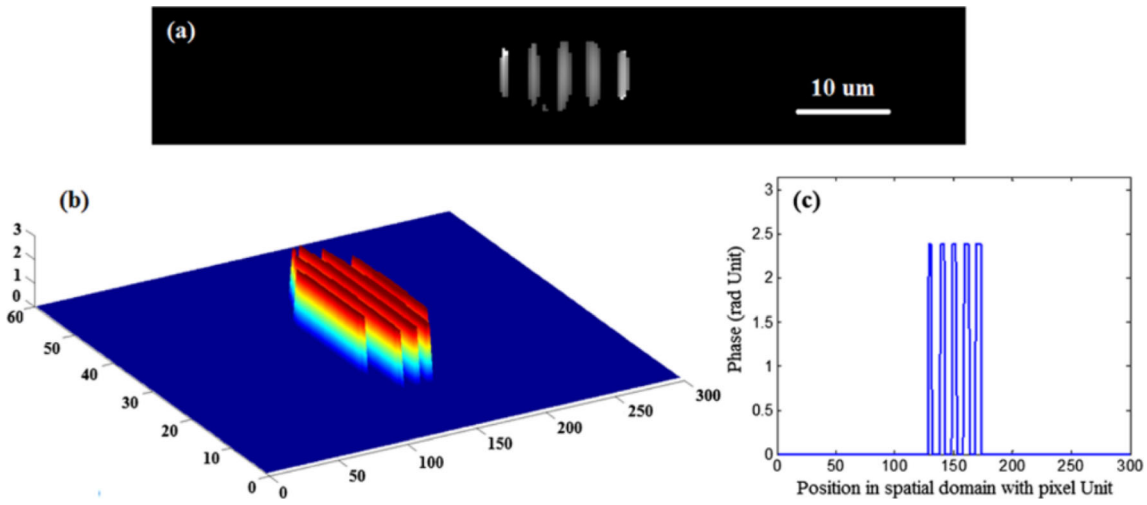

Fig. 26 (Color online) Amplitude (**a**) and phase (**b**) distributions of sample's transmittance retrieved from Fourier-transform diffraction patterns obtained in X-ray FGI; **c** profile of **b** [33]. Pixel size in the retrieved image was 0.297 μm

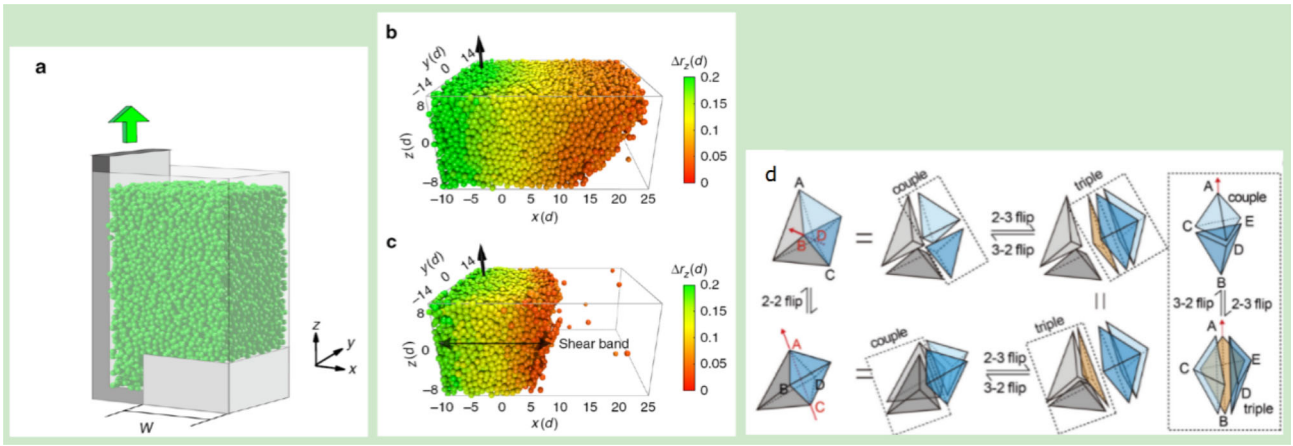

Fig. 27 (Color online) **a** Schematics of plane shear cell, **b**, **c** absolute z-displacement of each particle after first shear step and the steady states, respectively, **d** carrier of plasticity in amorphous materials [34]

rechargeable batteries. However, the microscopic process of metal electrodeposition and the role of additives are yet to be elucidated. The outstanding advantage of synchrotron radiation imaging is that it enables dynamic imaging in situ. Dynamic images of the solid/liquid interface can be effectively obtained throughout the metal electrodeposition process under different solution conditions by synchrotron radiation imaging [35–37]. Figure 28 shows images of evolution behaviors of zinc deposits in different electrolytes by in situ X-ray dynamic imaging [37]. The interfacial evolution behaviors show that the presence of reduced species containing mixed molecules in the inner coordination sphere benefits the formation of dense deposits for both nickel and zinc. Meanwhile, from the real-time images, it was discovered that imidazole-type ionic liquids as additives can improve the quality of zinc deposits in the ammoniacal electrolytes. The formation and growth of zinc dendrites were inhibited by the anions of ionic liquids, which could not easily coordinate with the zinc species.

The PDF method of the BL13W1 beamline can be used in the field of chemistry, enabling the efficient characterization of the microstructures of amorphous materials. Enzyme-amorphous metal–organic framework complexes were obtained by regulating the concentration of organic ligands during solution synthesis to produce metal ion ligand defects. The PDF of the material was further determined on the BL13W1; it was experimentally confirmed that the zinc ions and organic ligands in the amorphous metal–organic framework had a short-range to mid-range ordered coordination structure, and that they lacked a long-range ordered structure. Figure 29 shows the structures of the crystalline zeolitic imidazolate framework-8 (ZIF-8) (a) and amorphous zeolitic imidazolate framework

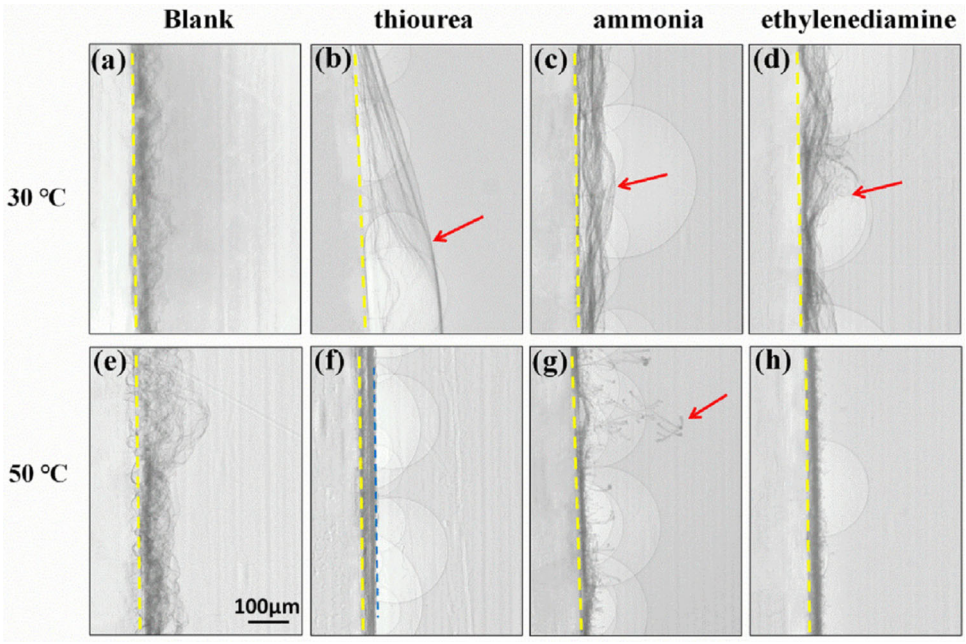

Fig. 28 Images of evolution behaviors of zinc deposits in different electrolytes at 30 °C and 50 °C by in situ X-ray dynamic imaging [37]. **a** Blank at 30 °C; **b** thiourea at 30 °C; **c** ammonia at 30 °C; **d** ethylenediamine at 30 °C; **e** blank at 50 °C; **f** thiourea at 50 °C; **g** ammonia at 50 °C; **h** ethylenediamine at 50 °C

(aZIF) (b) by molecular simulations (insets: schemes showing coordination), X-ray total scattering data (c), and PDF (d) of aZIF and ZIF-8. Figure 29e shows the enzymatic activities of enzyme-ZIF-8 and enzyme-incorporated aZIF [38]. The conclusions are essential for the rational interpretation of the efficient catalytic performances of the amorphous metal–organic framework complexes and provide reliable experimental evidence of the microscopic coordination structure of the amorphous metal–organic framework materials.

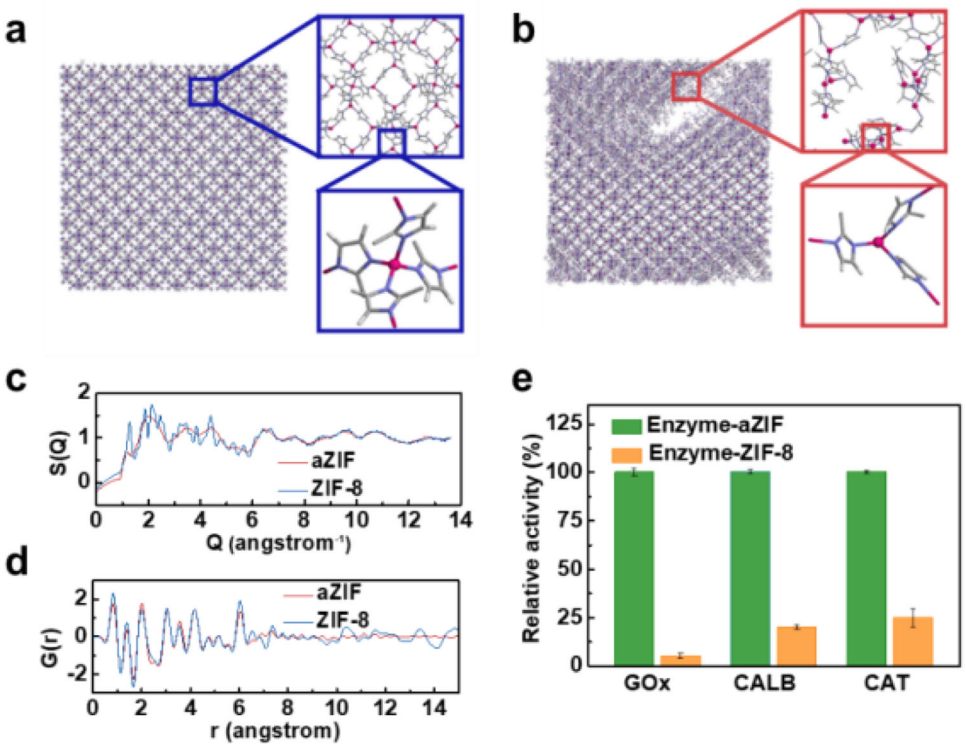

Fig. 29 (Color online) Structures of crystalline zeolitic imidazolate framework-8 (ZIF-8) (**a**) and amorphous zeolitic imidazolate framework (aZIF) (**b**) by molecular simulations (insets: schemes showing coordination), X-ray total scattering data (**c**), and PDF (**d**) of aZIF and ZIF-8, **e** enzymatic activities of enzyme-ZIF-8 and enzyme-incorporated aZIF [38]

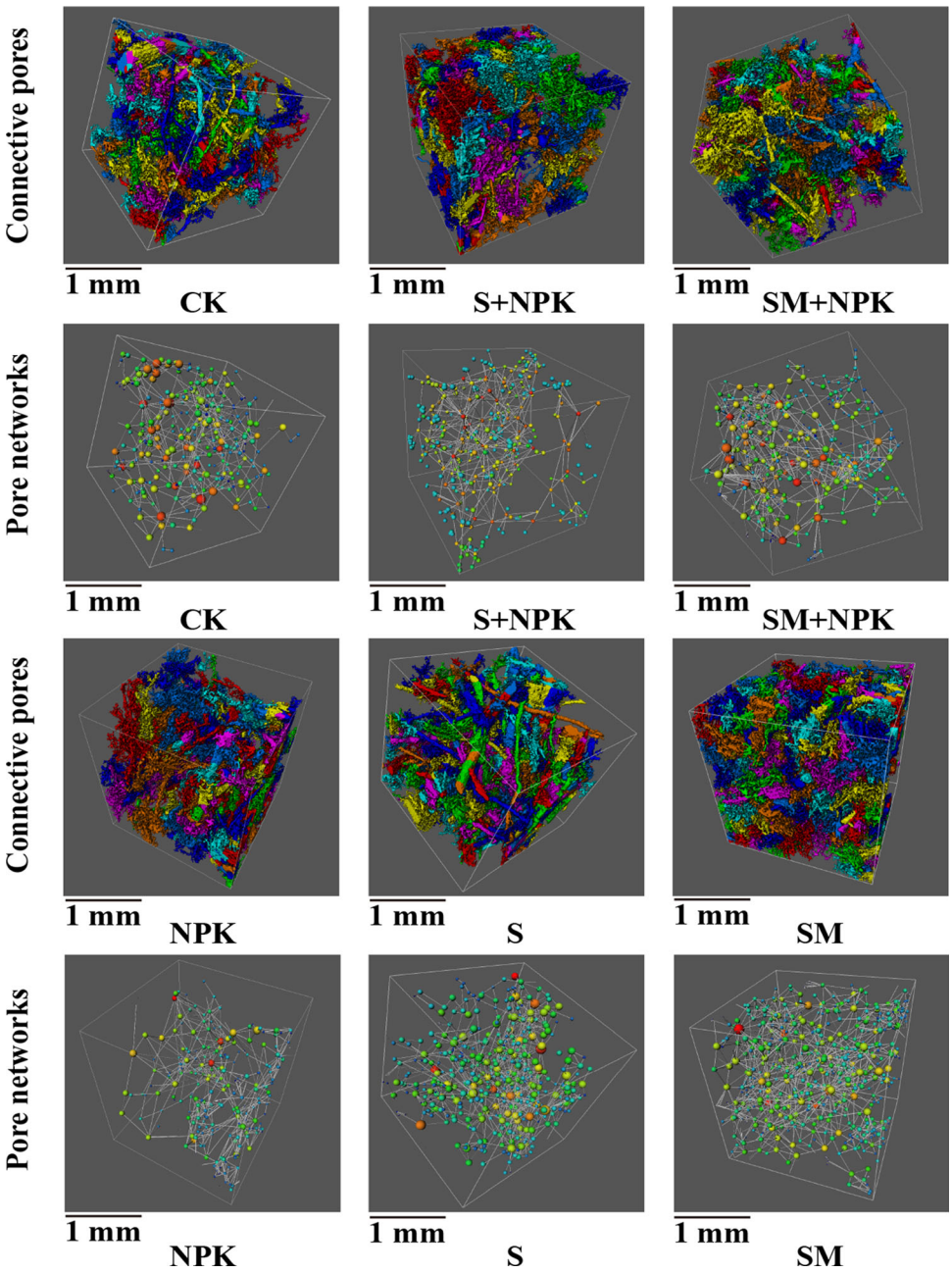

Fig. 30 (Color online) Thirty 3D pore structures of soils aggregates in different fertilization managements [40]

3.6 Environmental science

Soil aggregates are the basic unit of soil structure. They determine many physical, chemical, and biological processes occurring in soils and coordinate the soil fertility factors of water, air, and heat. A comprehensive investigation into the "black box" of intra-aggregates will contribute significantly to a better understanding of the process mechanism and carbon sequestration in soils. SR-μCT is a viable method to understand the "black box." It enables researchers to quantify the internal architecture of soil aggregates in three dimensions at multiple scales to understand the mechanisms of interaction between the aggregate pore structure and functions and to predict the response of the soil aggregate to environmental changes and management practices. For example, the effects of organic manure and chemical fertilizer on the pore network and microscale pore structure of soil aggregates can be effectively evaluated via SR-μCT and a pore network model [39, 40]. Figure 30 shows the 3D pore structures of soil aggregates in different fertilization managements via X-ray micro-CT [40].

Efficient dewatering treatment is an important prerequisite for the harmless disposal of sludge. Synchrotron

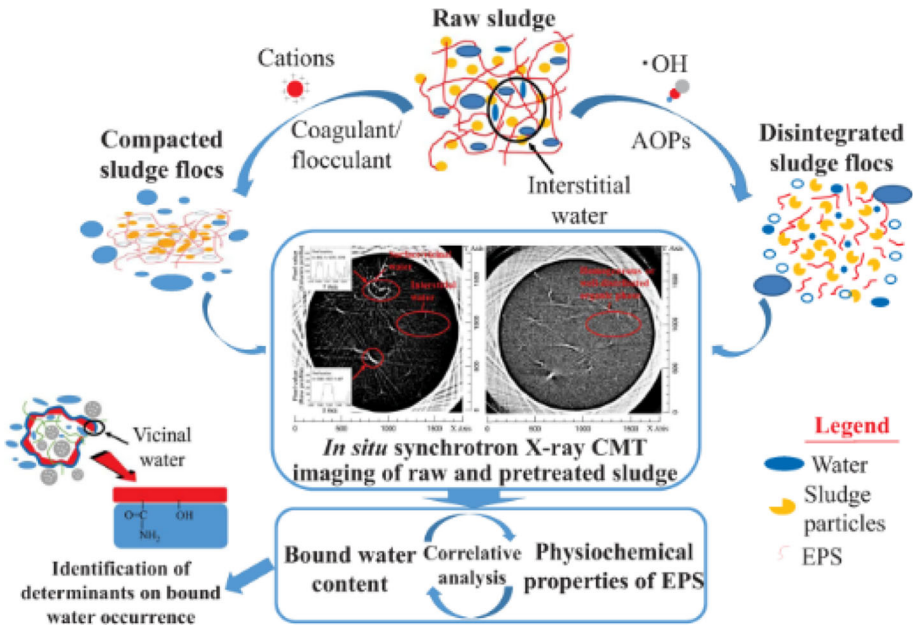

Fig. 31 (Color online) Sludge water migration conversion mechanism [41]

X-ray CT may enable the in situ analysis of the microstructure and water distribution patterns of sludge flocs and identification of key limiting factors of sludge dewatering. Figure 31 shows the images of the raw and pretreated sludge via SR-μCT and the sludge water migration conversion mechanism [41]. The results show that the primary sludge contains multiple aggregates independently dispersed in the liquid phase instead of the typically recognizable continuous homogeneous reticulated floc structure. Furthermore, the combined water reduction is the combined effect of hydrophilic material removal, extracellular polymer aggregate compression, and flocculation destabilization.

4 Summary

After 10 years of user operation, biomedical and material science applications on the BL13W1 beamline have demonstrated remarkable achievements. This applies to other fields such as archaeology, paleontology, pharmaceuticals, and environmental sciences as well. Micro-CT and dynamic imaging are dominant methods. Driven by user requirements, dynamic CT imaging has been developed. Micro-CT imaging combined with other X-ray experimental methods such as XRD, SAXS, and X-ray fluorescence are also being developed. A new X-ray imaging method known as MCXI has been proposed, with which blood flow and moving tissues in primary images can be distinguished according to their moving frequencies in the time domain. X-ray speckle-tracking imaging with twice exposure to eliminate the effect of edge enhancement has been developed. For complex 3D blood vessels obtained via X-ray tomography, a high-precision quantification method was realized. Additionally, an X-ray nano-CT experiment was performed with a 100 nm spatial resolution. The BL13W1 beamline is being upgraded currently. A super bending magnet source with 2.293 T magnetic field intensity and a double multilayer monochromator will be used on the beamline to provide a white beam and a monochromatic beam for different experiments. Moreover, two new X-ray imaging beamlines, named the "X-ray fast imaging beamline" and the "X-ray nano-CT beamline" in the phase-II project of SSRF, are being constructed. The X-ray fast imaging beamline will provide X-ray imaging techniques with various temporal resolutions from milliseconds, microseconds, to 100 ps as well as micrometer spatial resolutions for fast processes. The photon energy range is 8.7–30 keV. The beamline construction and commissioning will be completed by mid-2021. The BL18B beamline with a photon energy range of 5–14 keV based on a bending magnet is being built in the second-phase project of SSRF; the goal is to visualize the nanoscale internal structure in three dimensions. Design goals with the highest spatial resolution of 20–30 nm were proposed at 8 keV. The beamline and the TXM end-station construction and commissioning will be completed by mid-2021. The upgrading of the BL13W1 beamline and two new beamlines will provide users complete X-ray imaging methods with different spatial resolutions and temporal resolutions.

References

1. H.L. Xie, B. Deng, G.H. Du et al., Latest advances of X-ray imaging and biomedical applications beamline at SSRF. Nucl. Sci. Tech. **26**, 020102 (2015). https://doi.org/10.13538/j.1001-8042/nst.26.020102
2. L. Xu, R.C. Chen, G.H. Du et al., Anisotropic shrinkage of insect air sacs revealed in vivo by X-ray microtomography. Sci. Rep. **6**, 32380 (2016). https://doi.org/10.1038/srep32380
3. R.C. Chen et al., PITRE: software for phase-sensitive X-ray image processing and tomography reconstruction. J. Synchrotron Radiat. **19**, 836–845 (2012). https://doi.org/10.1107/S0909049512029731
4. H.L. Xie, H.X. Luo, G.H. Du et al., High-efficiency fast X-ray imaging detector development at SSRF. J. Synchrotron Radiat. **26**, 1631–1637 (2019). https://doi.org/10.1107/S1600577519010075
5. H.L. Xie, G.H. Du, B. Deng et al., Study of Scintillator thickness optimization of lens-coupled X-ray imaging detectors. J. Instrum. **11**, C03057 (2016). https://doi.org/10.1088/1748-0221/11/03/C03057
6. B.G. Feng, F. Tao, Y.-M. Yang et al., X-ray fluorescence microtomography based on polycapillary focused X-rays from laboratory source. Nucl. Sci. Tech. **29**(6), 85 (2018). https://doi.org/10.1007/s41365-018-0417-x
7. P.F. Sun, B. Deng, G.H. Du et al., Nondestructive rare earth element imaging of fish teeth from deep-sea sediments. X-Ray Spectrom. **44**, 442–446 (2015). https://doi.org/10.1002/xrs.2624
8. B. Deng, G.H. Du, G.Z. Zhou et al., 3D elemental sensitive imaging by full-field XFCT. Analyst **140**, 3521–3525 (2015). https://doi.org/10.1039/C4AN02401J
9. D.J. Jensen, Chap 15: 4D characterization of metal microstructures, materials science and characterization. Dep. Wind Energy (2013). https://doi.org/10.1002/9783527652815.ch15
10. Y.M. Yang, L. Xu, Y.D. Wang et al., Non-destructive identification of unknown minor phases in polycrystalline bulk alloys using three-dimensional X-ray diffraction. Mater. Charact. **124**, 206–214 (2017). https://doi.org/10.1016/j.matchar.2016.12.025
11. T. Hu, Y.D. Wang, G.H. Du et al., Improving the efficiency of small-angle X-ray scattering computed tomography using the OSEM algorithm. Appl. Opt. **56**(30), 8326–8334 (2017). https://doi.org/10.1364/AO.56.008326
12. T. Hu, W.Q. Hua, G.J. Zhong et al., Nondestructive and quantitative characterization of bulk injection molded polylactide using SAXS microtomography. Macromolecules (2020). https://doi.org/10.1021/acs.macromol.0c01177
13. B.G. Feng, B. Deng, Y.Q. Ren et al., Full-field X ray nano-imaging system designed and constructed at SSRF. Chin. Opt. Lett. **14**(9), 093401-0-05 (2016). https://doi.org/10.1117/12.2035589
14. Y.D. Wang, Y.Q. Ren, G.Z. Zhou et al., Equally sloped tomography based X-ray full-field nano-CT at Shanghai Synchrotron Radiation Facility. Nucl. Instrum. Methods Phys. Res. A **896**, 108–112 (2018). https://doi.org/10.1016/j.nima.2018.04.024
15. F.X. Wang, P.T. Zhou, K. Li et al., Sensitive imaging of intact microvessels in vivo with synchrotron radiation. IUCrJ (2020). https://doi.org/10.1107/S2052252520008234
16. F.X. Wang, Y.D. Wang, G.X. Wei et al., Speckle-tracking X-ray phase-contrast imaging for samples with obvious edge enhancement effect. Appl. Phys. Lett. **111**, 174101 (2017). https://doi.org/10.1063/1.4997970
17. Z.H. Hu, M. Sun, M. Lv et al., Deciphering buried air phase on natural and bioinspired superhydrophobic surfaces using synchrotron radiation-based X-ray phase-contrast imaging. NPG Asia Mater. **8**, e306 (2016). https://doi.org/10.1038/am.2016.122
18. W. Tang, D. Lin, Y.M. Yu et al., Bioinspired trimodal macro/micro/nano-porous scaffolds loading rhBMP-2 for complete regeneration of critical size bone defect. Acta Biomater. **32**, 309–323 (2016). https://doi.org/10.1016/j.actbio.2015.12.006
19. Y.F. Ma, W.J. Zhang, Z.H. Wang et al., PEGylated poly(glycerol sebacate)-modified calcium phosphate scaffolds with desirable mechanical behavior and enhanced osteogenic capacity. Acta Biomater. **44**, 110–124 (2016). https://doi.org/10.1016/j.actbio.2016.08.023
20. Y.T. Liu, Y.F. Ma, J. Zhang et al., MBG-modified β-TCP scaffold promotes mesenchymal stem cells adhesion and osteogenic differentiation via a FAK/MAPK signaling pathway. ACS Appl. Mater. Interfaces. **9**, 30283–30296 (2017). https://doi.org/10.1021/acsami.7b02466
21. L.S. Cai, D. Lin, Y.J. Chai et al., MBG scaffolds containing chitosan microspheres for binary delivery of IL-8 and BMP-2 for bone regeneration. J. Mater. Chem. B **6**, 4453 (2018). https://doi.org/10.1039/C8TB00875B
22. H. Wu, G.H. Fan, M. Huang et al., Deformation behavior of brittle/ductile multilayered composites under interface constraint effect. Int. J. Plast **89**, 96–109 (2017). https://doi.org/10.1016/j.ijplas.2016.11.005
23. M. Huang, C. Xu, G.H. Fan et al., Role of layered structure in ductility improvement of layered Ti–Al metal composite. Acta Mater. **153**, 235–249 (2018). https://doi.org/10.1016/J.ACTAMAT.2018.05.005
24. K. Li, B. Deng, H.P. Zhang et al., Comprehensive characterization of TSV etching performance with phase-contrast X-ray microtomography. J. Synchrotron Radiat. (2020). https://doi.org/10.1107/S1600577520005494
25. Q. Yu, X.D. Wang, H.B. Lou et al., Atomic packing in Fe-based metallic glasses. Acta Mater. **102**, 116–124 (2016). https://doi.org/10.1016/j.actamat.2015.09.001
26. J.X. Wang, X.J. Lin, Z.H. Mu et al., Rapamycin increases collateral circulation in rodent brain after focal ischemia as detected by multiple modality dynamic imaging. Theranostics **9**, 4923–4934 (2019). https://doi.org/10.7150/thno.32676
27. S.F. Ni, Z.X. Luo, L.Y. Jiang et al., UTX/KDM6A deletion promotes recovery of spinal cord injury by epigenetically regulating vascular regeneration. Mol. Ther. **27**, 2134–2146 (2019). https://doi.org/10.1016/j.ymthe.2019.08.009
28. H. Tan, D.D. Wang, R.X. Li et al., A robust method for high-precision quantification of the complex three-dimensional vasculatures acquired by X-ray microtomography. J. Synchrotron Radiat. (2016). https://doi.org/10.1107/S1600577516011498
29. L. Zhang, L. Wu, C.F. Wang et al., Synchrotron radiation microcomputed tomography guided chromatographic analysis for displaying the material distribution in tablets. Anal. Chem. **90**, 3238–3244 (2018). https://doi.org/10.1021/acs.analchem.7b04726
30. L.D. Xing, R.C. McKellar et al., Mummified precocial bird wings in mid-Cretaceous Burmese amber. Nat. Commun. **7**, 12089 (2016). https://doi.org/10.1038/ncomms12089
31. S. Wang, J. Stiegler, R. Amiot et al., Extreme ontogenetic changes in a ceratosaurian theropod. Curr. Biol. **27**, 1–5 (2017). https://doi.org/10.1016/j.cub.2016.10.043
32. S. Wang, J. Stiegler, P. Wu et al., Heterochronic truncation of odontogenesis in theropod dinosaurs provides insight into the macroevolution of avian beaks. Proc. Natl. Acad. Sci. U. S. A. **114**, 10930 (2017). https://doi.org/10.1073/pnas.1708023114
33. H. Yu, R.H. Lu, S.S. Han et al., Fourier-transform ghost imaging with hard X rays. Phys. Rev. Lett. **117**, 113901 (2016). https://doi.org/10.1103/PhysRevLett.117.113901
34. Y.X. Cao, J.D. Li, B.Q. Kou et al., Structural and topological nature of plasticity in sheared granular materials. Nat. Commun. **9**, 2911 (2018). https://doi.org/10.1038/s41467-018-05329-8

35. Y.X. Song, J. Tang, J.G. Hua et al., Insights into electrodeposition process of nickel from ammonium chloride media with speciation analysis and in situ synchrotron radiation X-ray imaging. Electrochim. Acta **210**, 812–820 (2016). https://doi.org/10.1016/j.electacta.2016.06.033
36. Y. Song, J. Hu, J. Tang et al., Real-time X-ray imaging reveals interfacial growth, suppression, and dissolution of zinc dendrites dependent on anions of ionic liquid additives for rechargeable battery applications. ACS Appl. Mater. Interfaces. **8**, 32031–32040 (2016). https://doi.org/10.1021/acsami.6b11098
37. Y.X. Song, J. Tang, J.G. Hua, Interfacial assistant role of amine additives on zinc electrodeposition from deep eutectic solvents: an in situ X-ray imaging investigation. Electrochim. Acta **240**, 90–97 (2017). https://doi.org/10.1016/j.electacta.2017.04.063
38. X.L. Wu, H. Yue, Y.Y. Zhang et al., Packaging and delivering enzymes by amorphous metal-organic frameworks. Nat. Commun. **10**, 5165 (2019). https://doi.org/10.1038/s41467-019-13153-x
39. X. Yu, C. Hong, G. Peng et al., Response of pore structures to long-term fertilization by a combination of synchrotron radiation X-ray microcomputed tomography and a pore network model. Eur. J. Soil Sci. **69**, 290–302 (2018). https://doi.org/10.1111/ejss.12513
40. S.G. Lu, X.L. Yu, Y.T. Zong, Nano-microscale porosity and pore size distribution in aggregates of paddy soil as affected by long-term mineral and organic fertilization under rice wheat cropping system. Soil Tillage Res. **186**, 191–199 (2019). https://doi.org/10.1016/j.still.2018.10.008
41. B.R. Wu, M. Zhou, X.H. Dai et al., Mechanism insights into bio-floc bound water transformation based on synchrotron X-ray computed microtomography and viscoelastic acoustic response analysis. Water Res. **142**, 480–489 (2018). https://doi.org/10.1016/j.watres.2018.06.003